The Role of Flexible Geothermal Power in Decarbonized Electricity Systems: Supplementary Information

Wilson Ricks[1] Katharine Voller[2] Gerame Galban[2] Jack H. Norbeck[2]
Jesse D. Jenkins[1]

[1]Princeton University
[2]Fervo Energy

Contents

Supplementary Note 1: Supplementary Figures

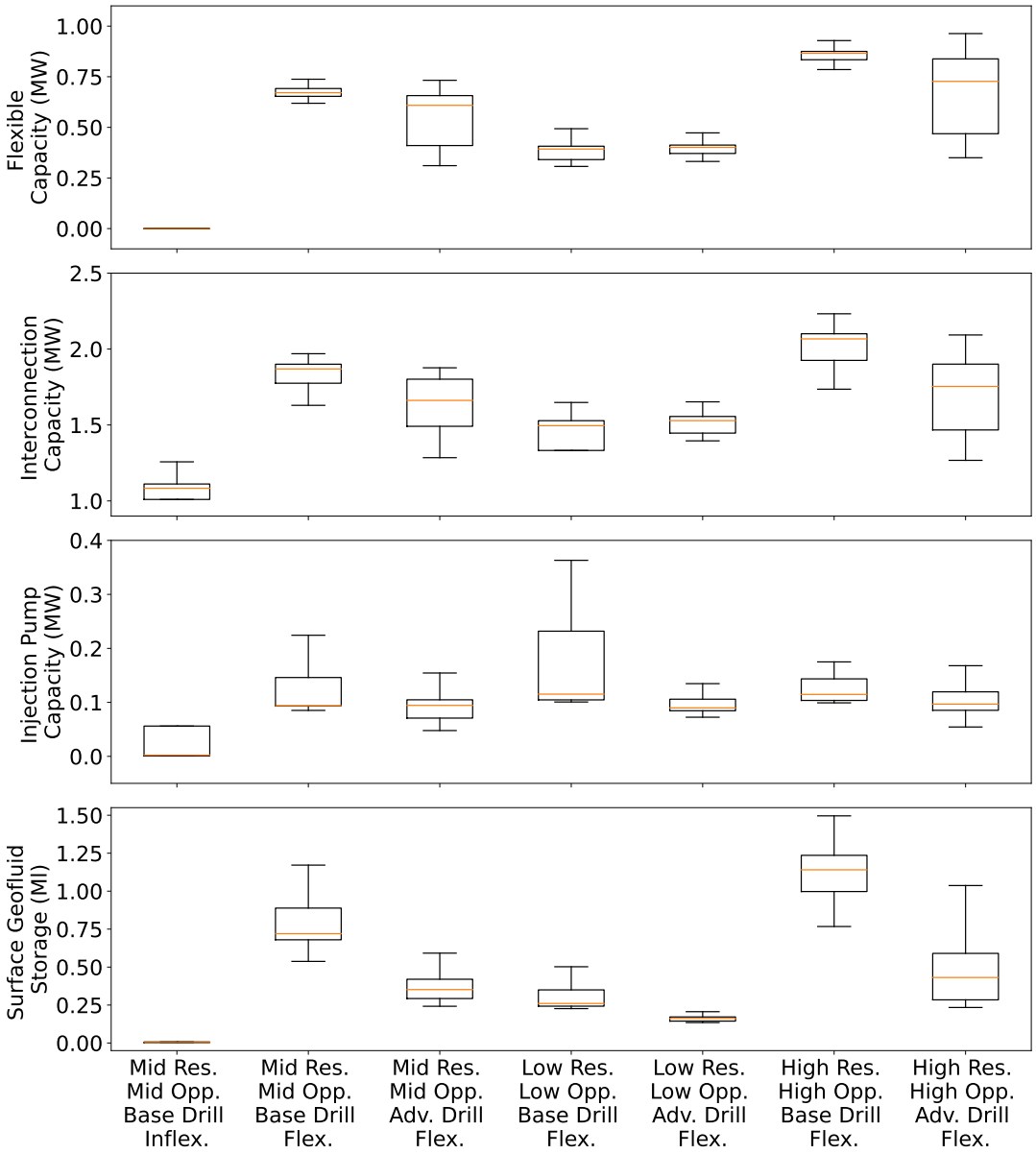

Supplementary Figure 1: Optimal EGS power plant configurations for a selection of model scenarios. Box plots indicate the relative sizing of flexible capacity, interconnection capacity, injection pump capacity, and surface geofluid storage per 1 MW of installed EGS baseload capacity. Orange lines indicate the capacity-weighted average value in each scenario. Boxes indicate the interquartile range (IQR), and whiskers indicate a further 1.5×IQR. Relative sizing of flexible components is largest in scenarios with low EGS penetration but high added value from flexibility.

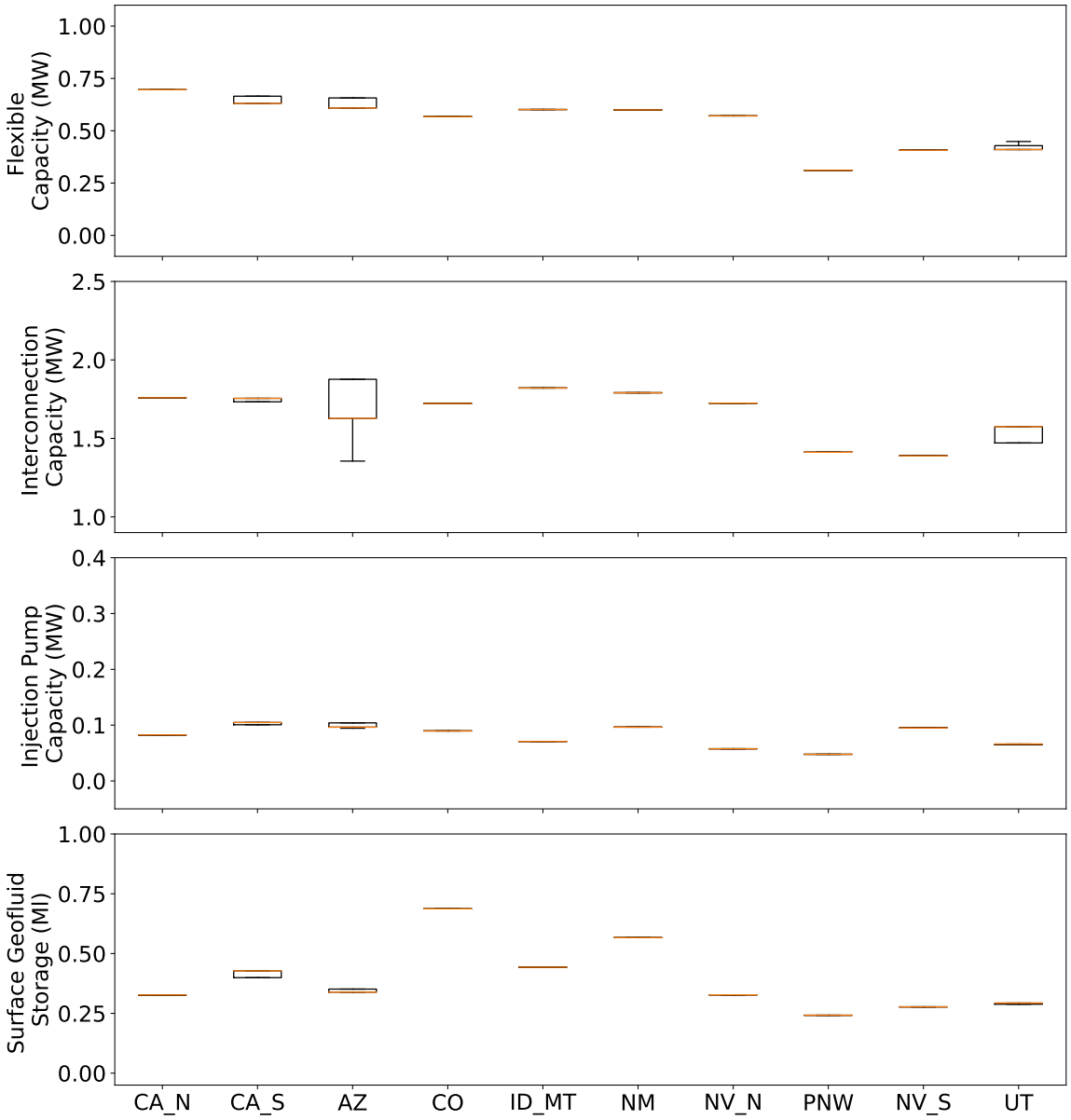

Supplementary Figure 2: Optimal flexible EGS power plant configurations by zone, for plants at 6.5 km exploiting a 250 °C resource, in the scenario with advanced geothermal drilling and mid-case market opportunity and subsurface favorability. Box plots indicate the relative sizing of flexible capacity, interconnection capacity, injection pump capacity, and surface geofluid storage per 1 MW of installed EGS baseload capacity. Orange lines indicate the capacity-weighted average value in each scenario. Boxes indicate the interquartile range (IQR), and whiskers indicate a further 1.5×IQR. Relative sizing of flexible components is fairly consistent across model zones, though plants in the Pacific northwest are configured to be less flexible.

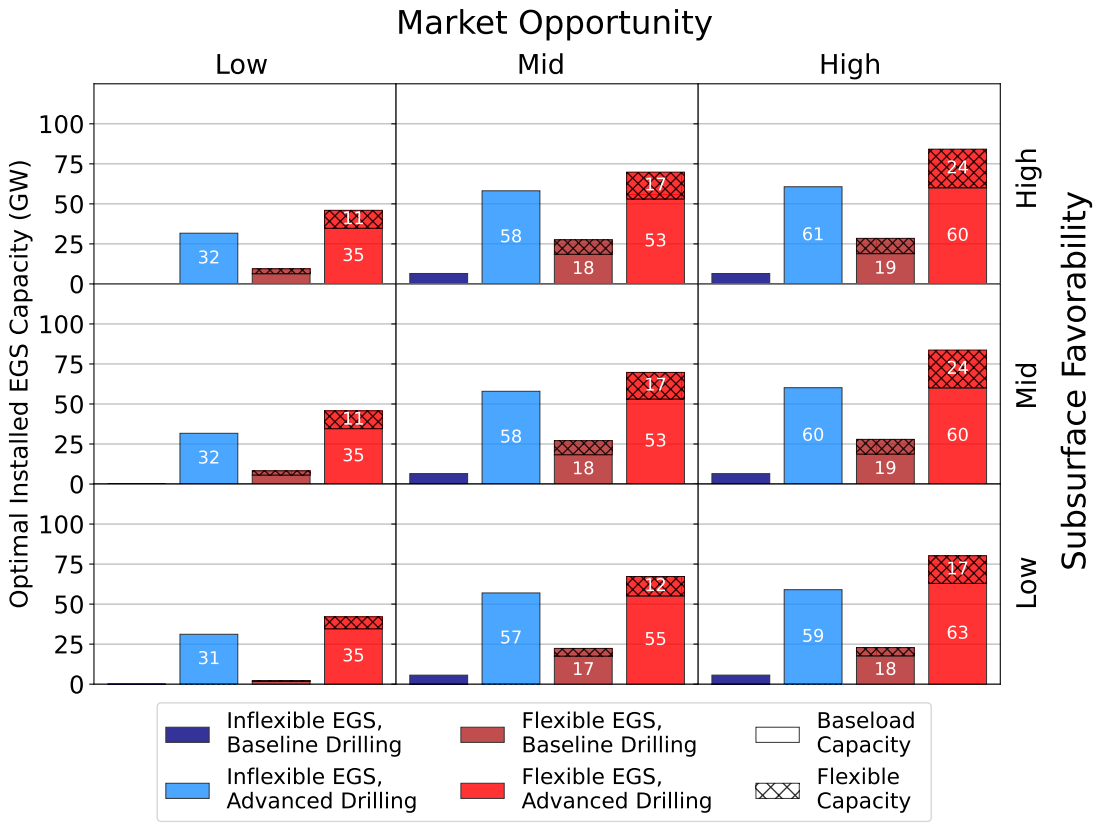

Supplementary Figure 3: EGS deployment potential in 90% decarbonized electricity systems. Same as Figure 2 in the main paper, for scenarios with a 90% clean electricity requirement. Data labels are provided for capacities greater than 10 GW.

Supplementary Figure 4: EGS deployment potential in 80% decarbonized electricity systems. Same as Figure 2 in the main paper, for scenarios with a 80% clean electricity requirement.Data labels are provided for capacities greater than 10 GW.

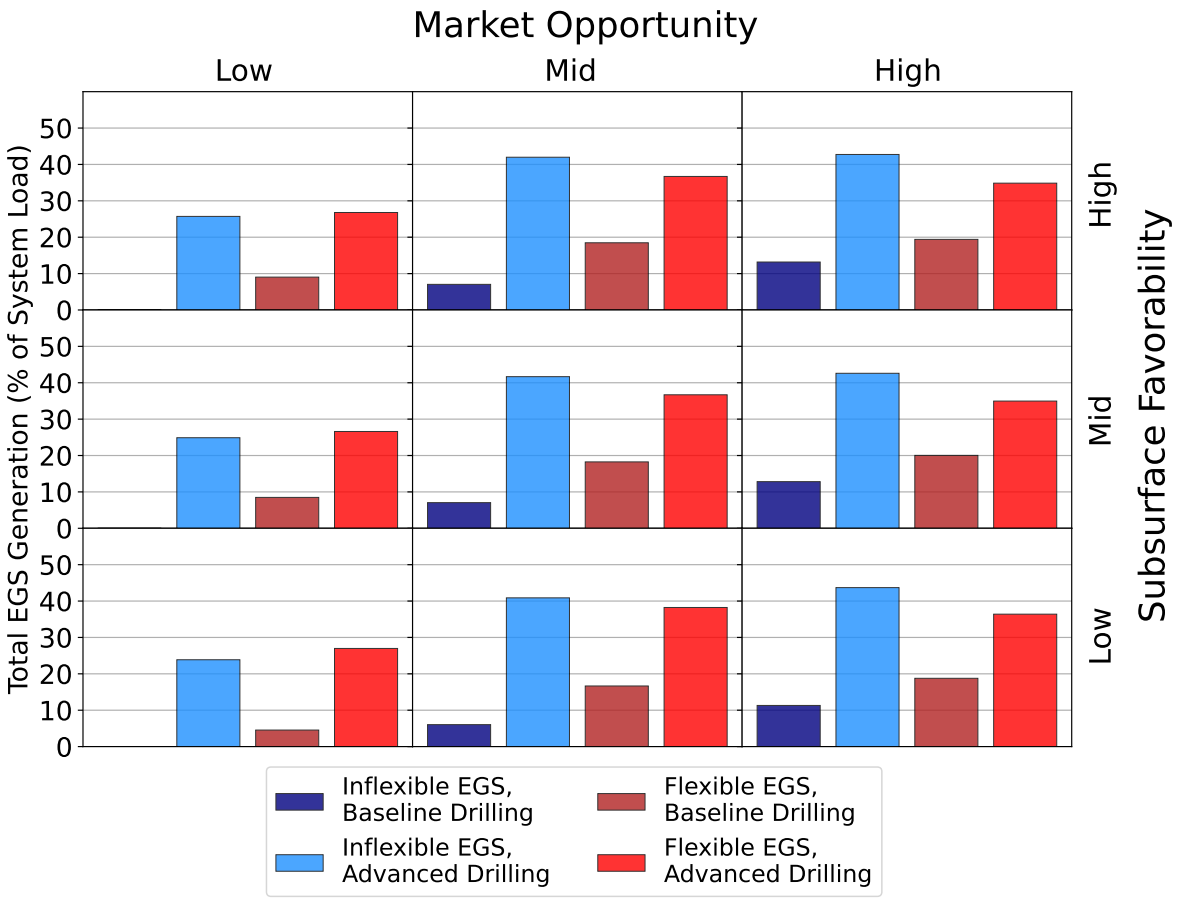

Supplementary Figure 5: Annual EGS generation as a percentage of total load under a range of scenarios combining EGS market opportunity, subsurface favorability, drilling, and flexibility cases, for fully-decarbonized systems.

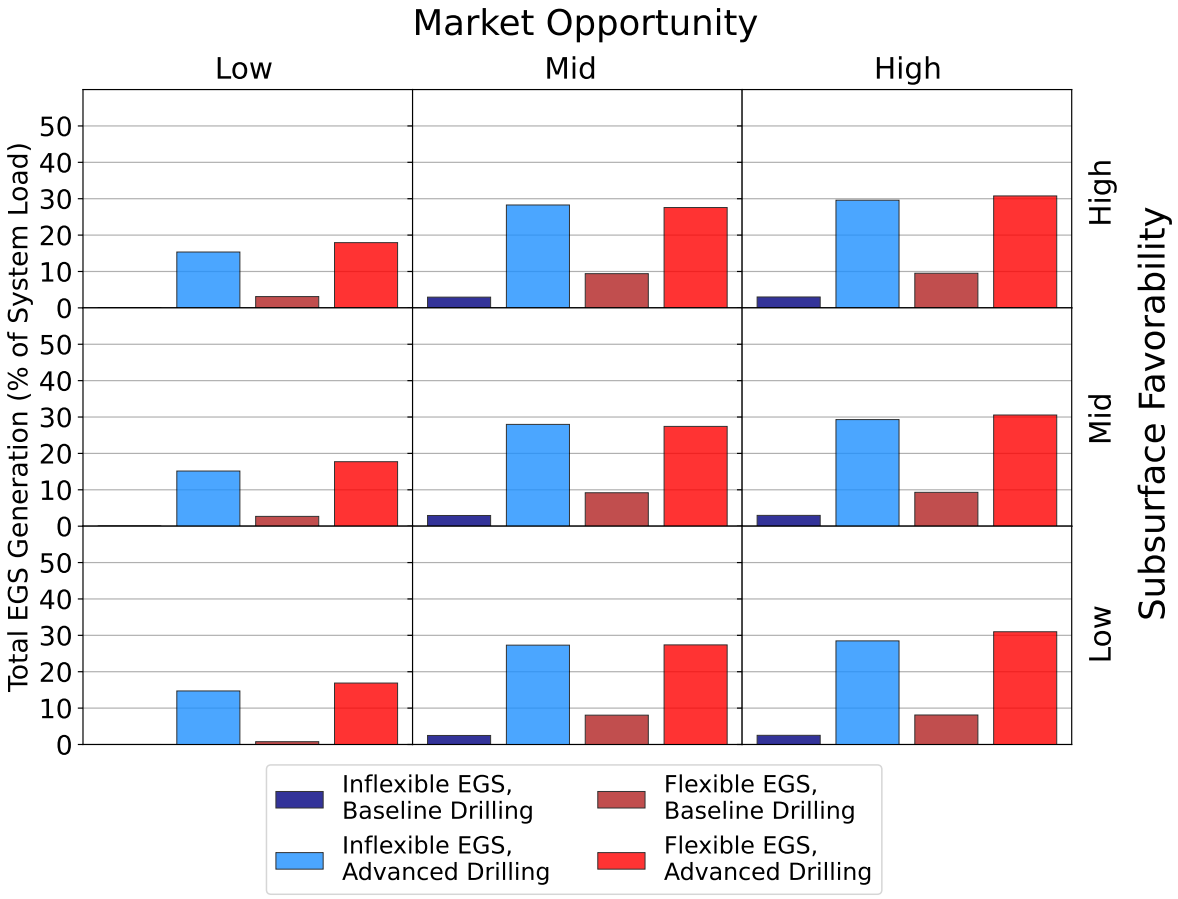

Supplementary Figure 6: Same as Supplementary Figure 5, for 90%-decarbonized systems.

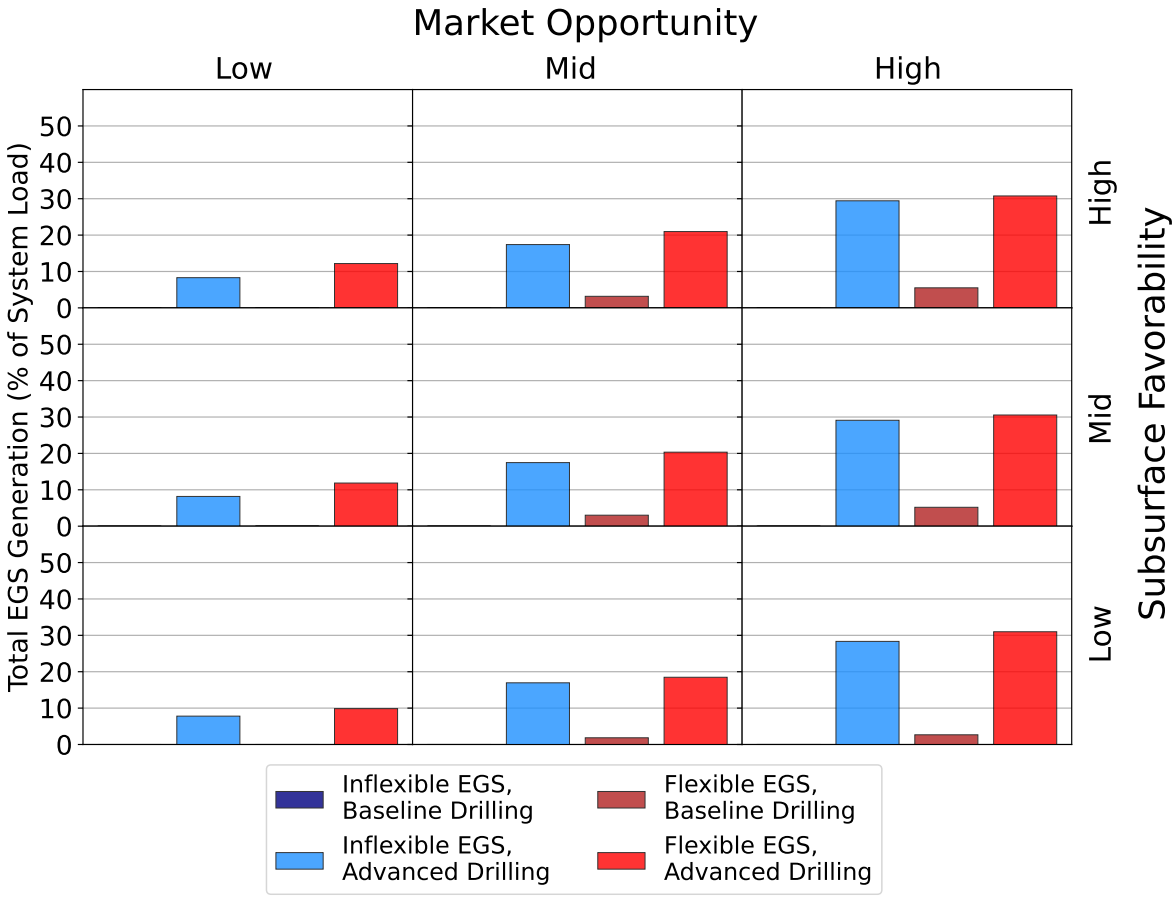

Supplementary Figure 7: Same as Supplementary Figure 5, for 80%-decarbonized systems.

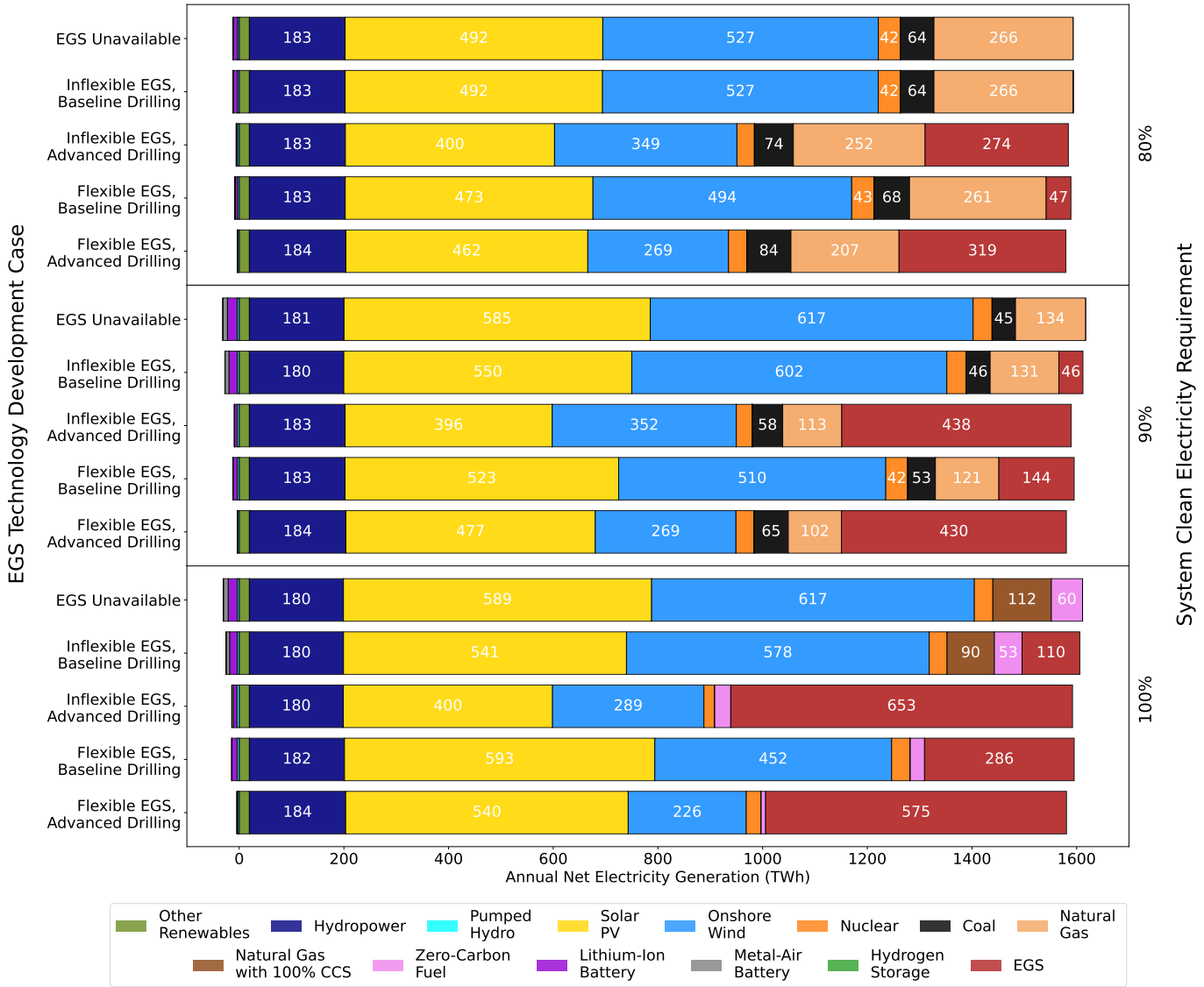

Supplementary Figure 8: Cost-optimal annual generation by technology and scenario for scenarios with mid-case EGS market opportunity and subsurface favorability. The right y-axis indicates the system-wide clean electricity requirement, represented as a percentage of total generation. Data labels are provided for values greater than 40 TWh.

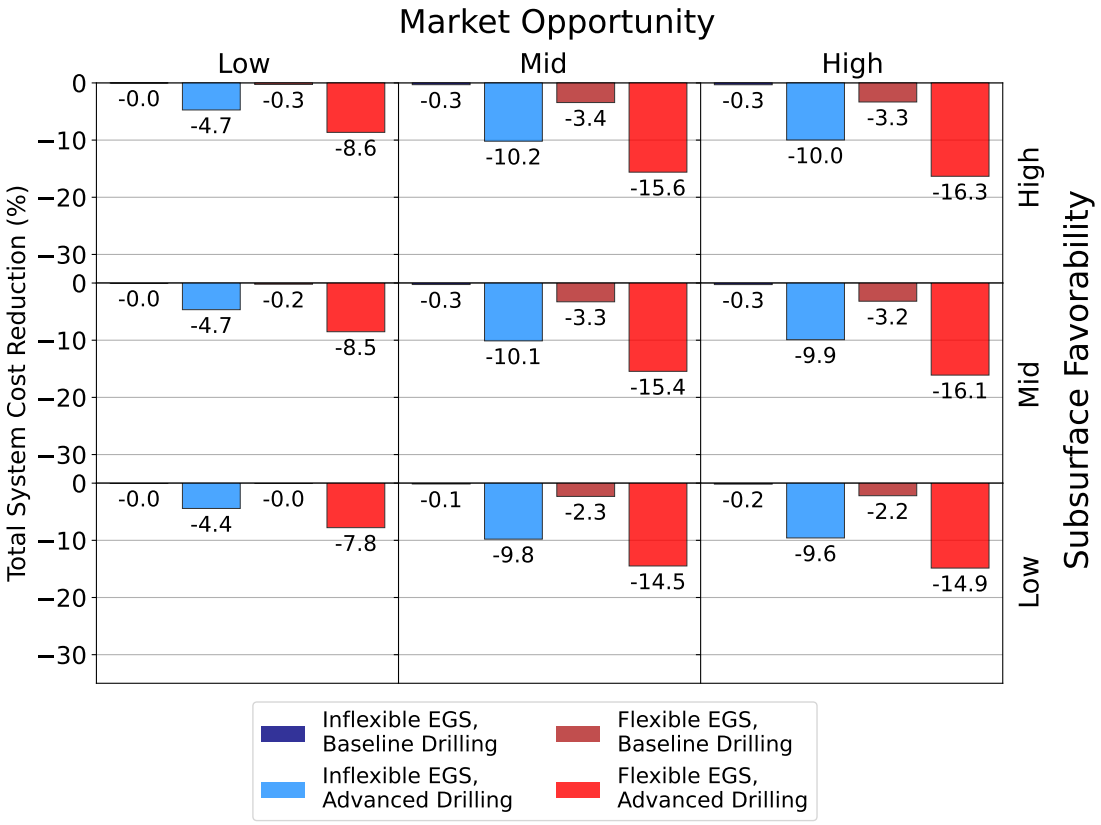

Supplementary Figure 9: Same as Figure 4 in the main paper, for 90%-decarbonized systems.

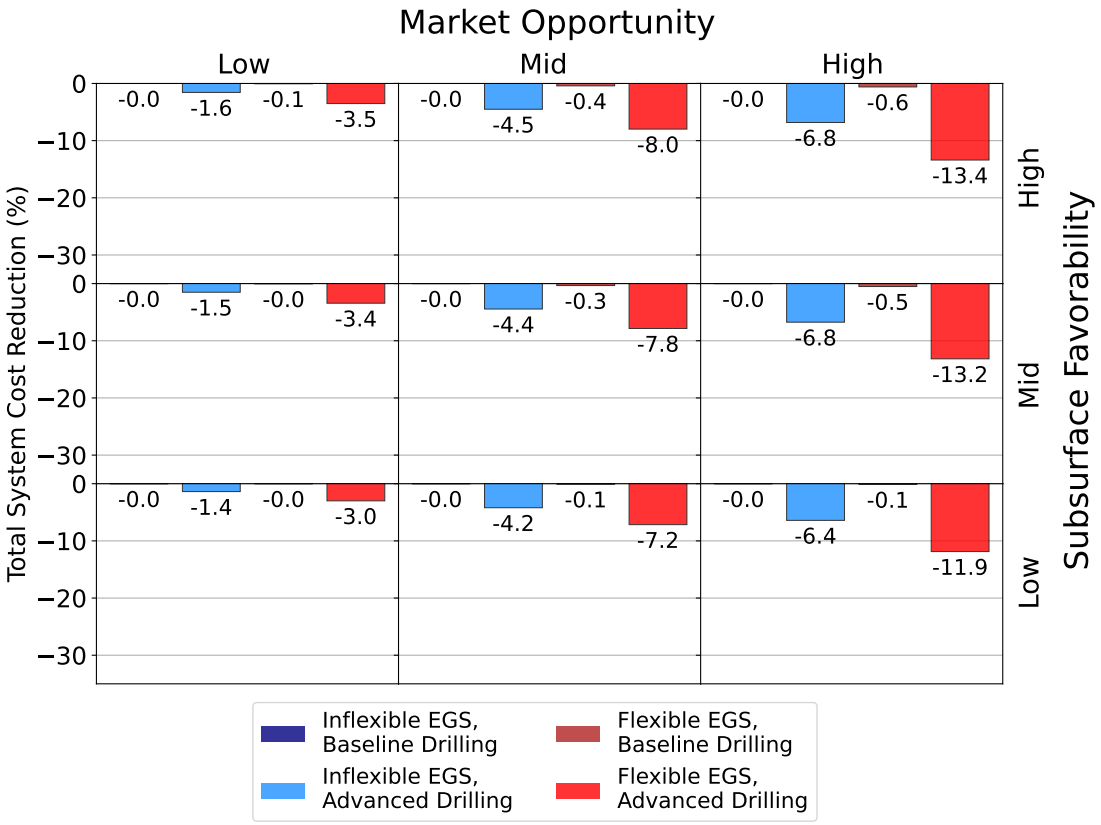

Supplementary Figure 10: Same as Figure 4 in the main paper, for 80%-decarbonized systems.

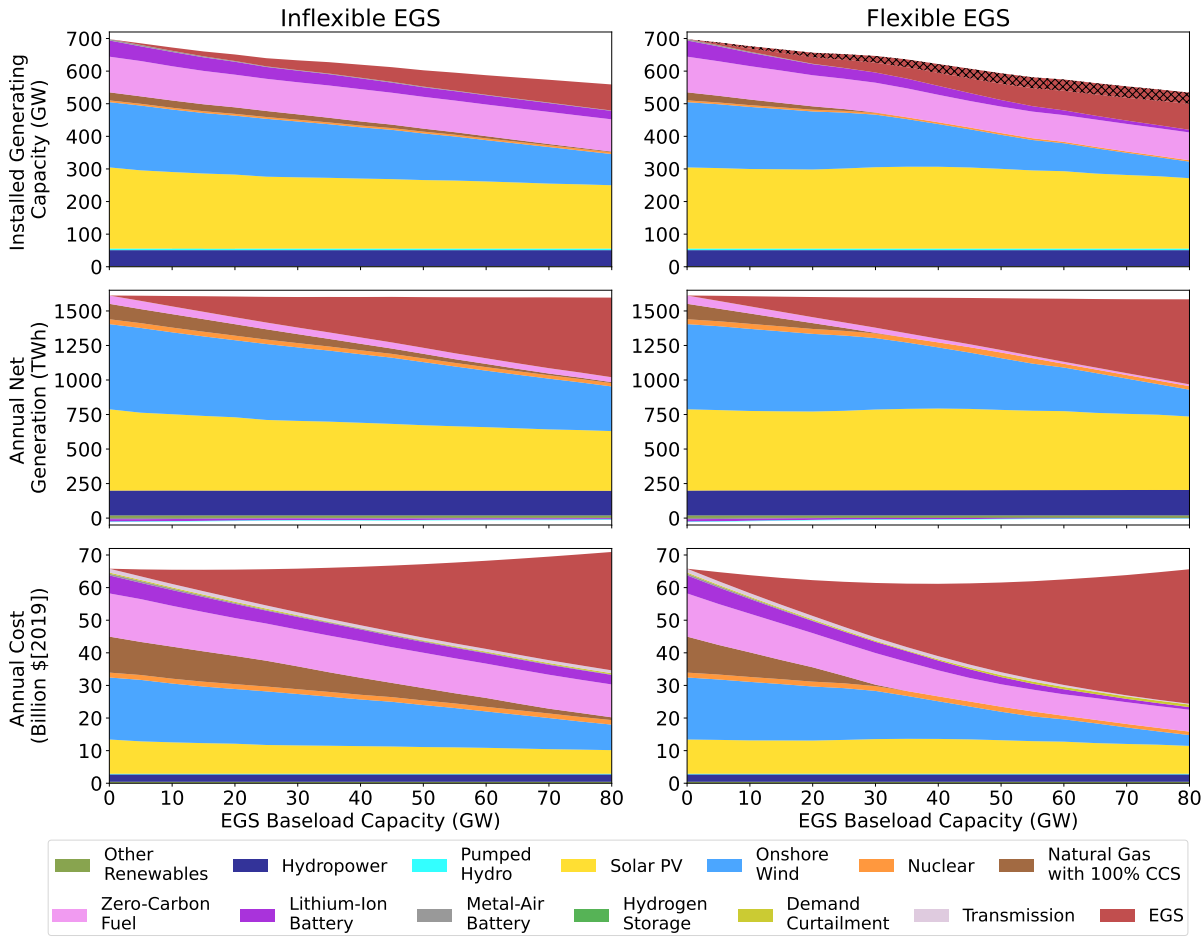

Supplementary Figure 11: Same as Figure 5 in the main paper, for EGS with baseline drilling.

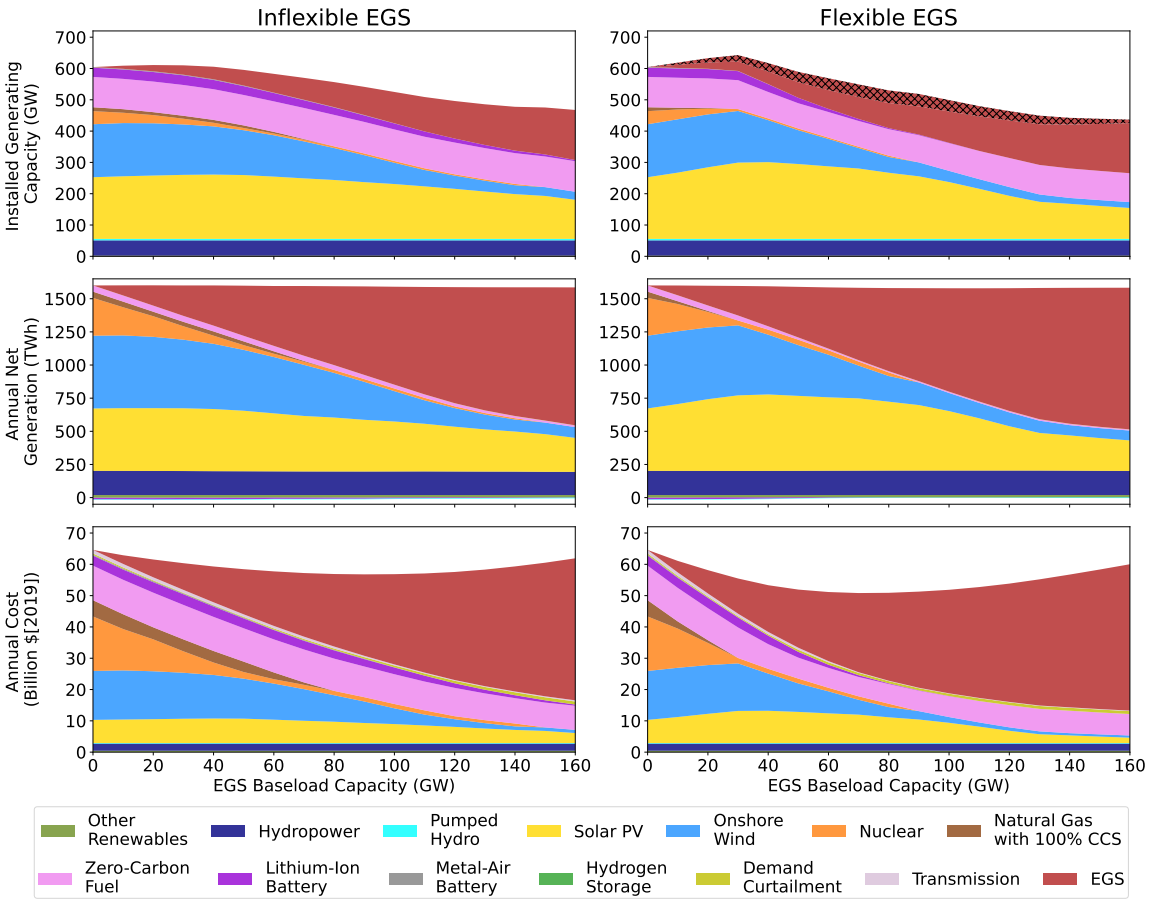

Supplementary Figure 12: Same as Figure 5 in the main paper, but with advanced nuclear costs set to the 'low' value of $4311/kW.

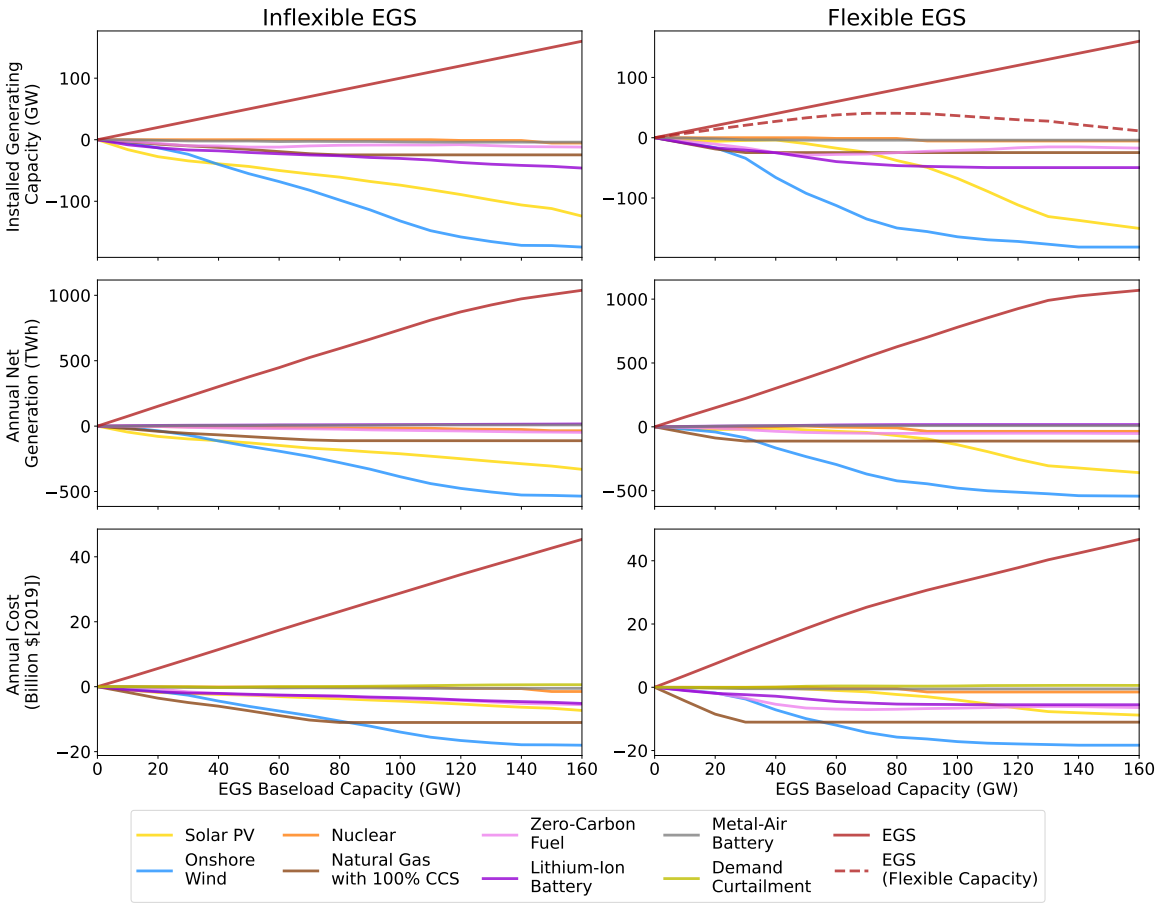

Supplementary Figure 13: Changes in installed capacity, net generation, and system cost contribution of selected technologies compared to systems with no EGS, as a function of baseload EGS capacity, for systems with inflexible and flexible EGS. Scenarios assume mid-case market opportunity and subsurface favorability, and advanced drilling.

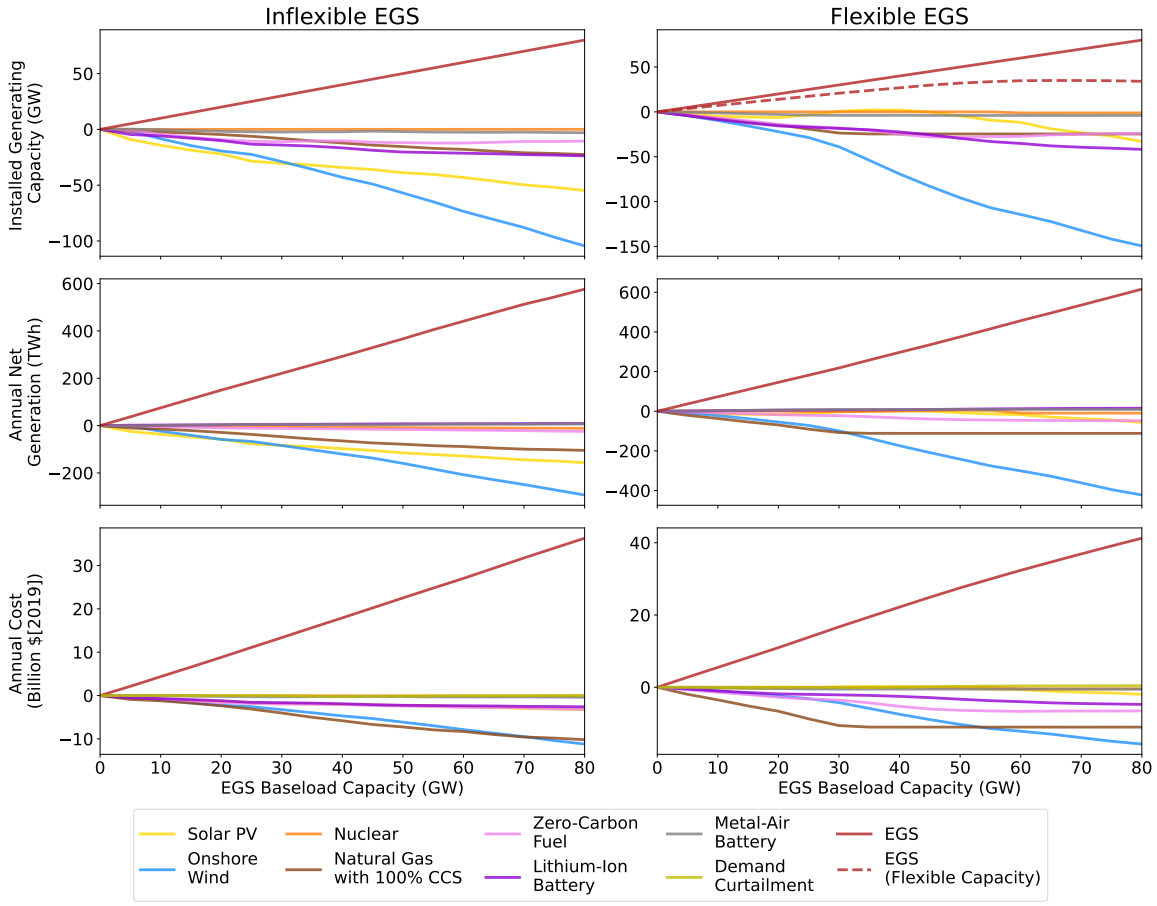

Supplementary Figure 14: Same as Supplementary Figure 13, for EGS with baseline drilling.

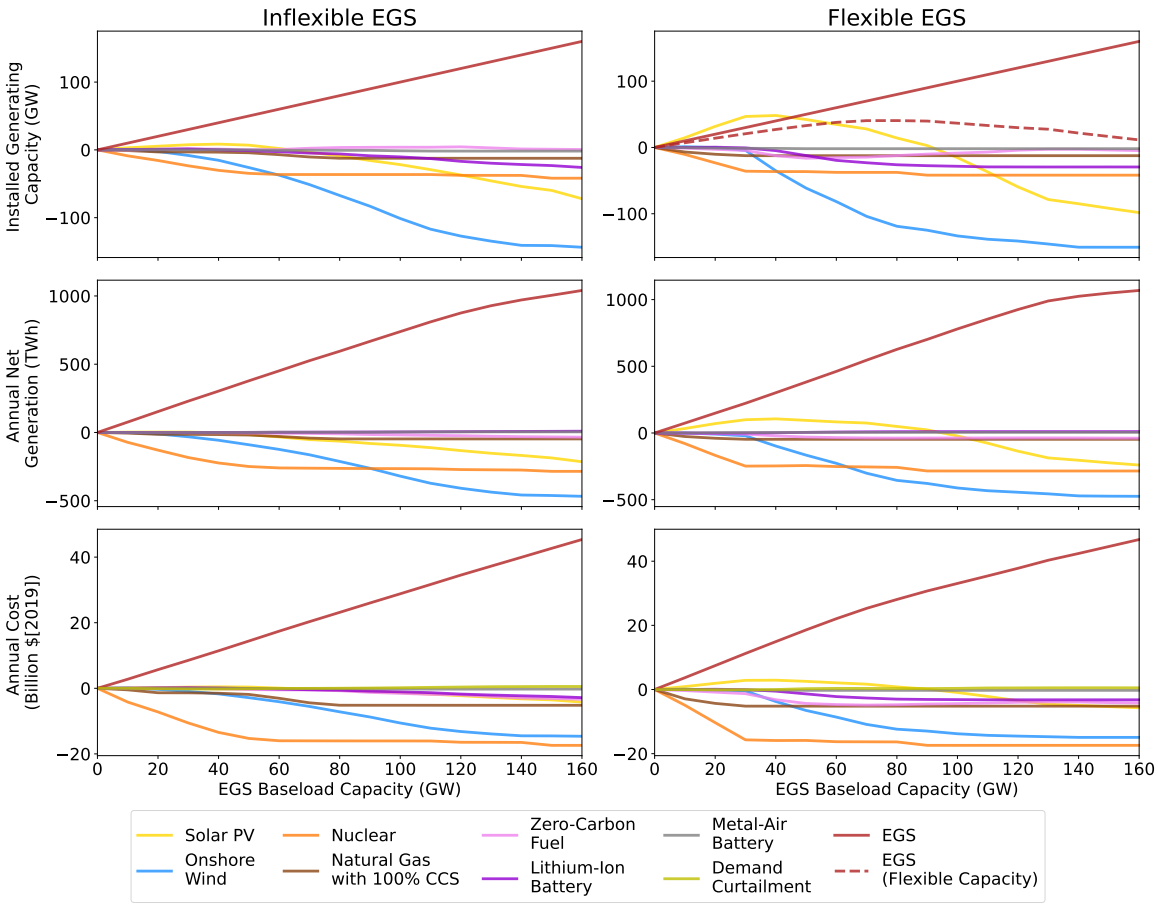

Supplementary Figure 15: Same as Supplementary Figure 13, but with advanced nuclear costs set to the 'low' value of $4311/kW.

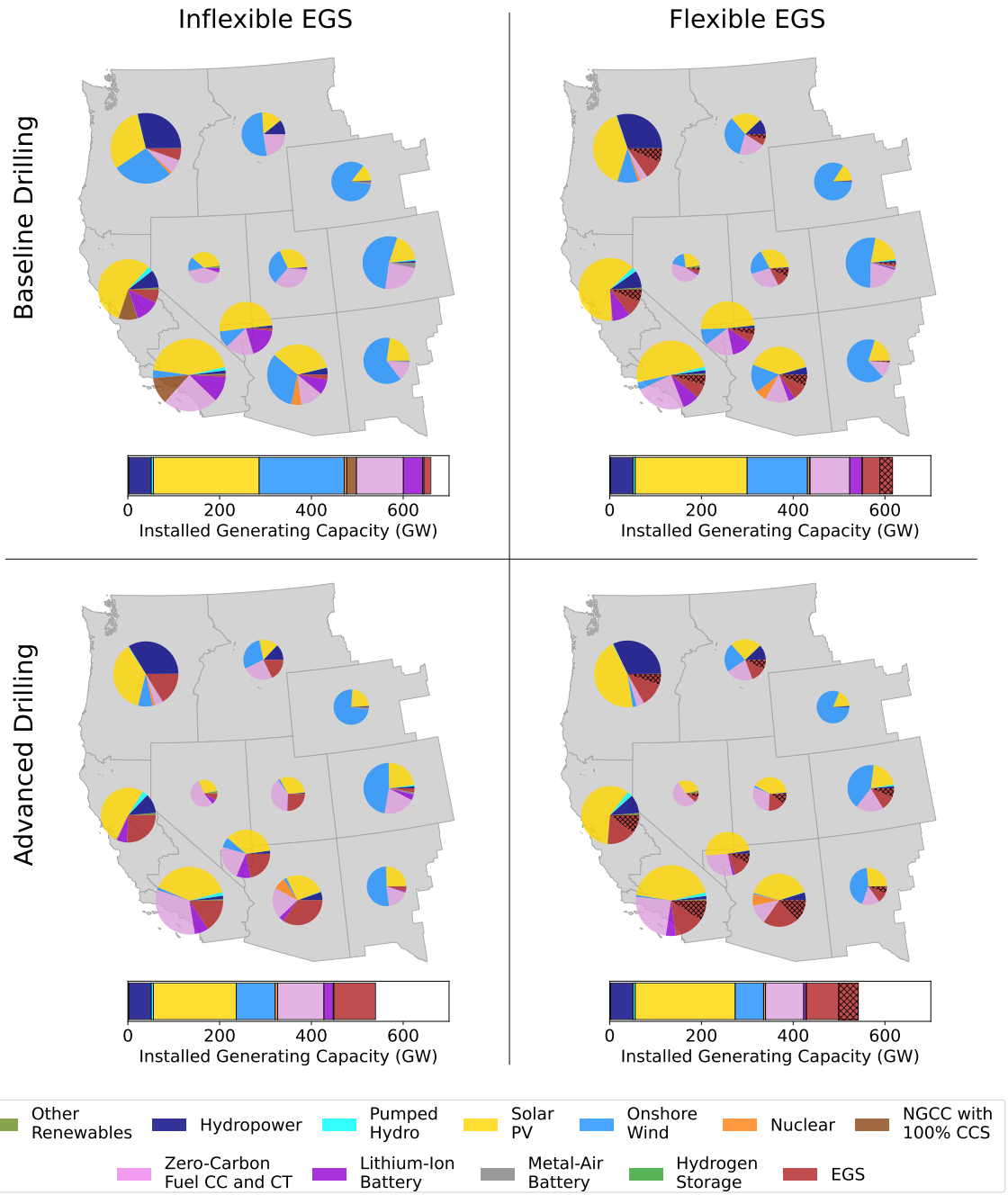

Supplementary Figure 16: Cost-optimal installed capacities by technology and model zone for scenarios with mid-case market opportunity and subsurface favorability. Scenarios assuming inflexible and flexible EGS with baseline and advanced drilling are shown. Zonal capacities scale with pie chart area, and crosshatches indicate flexible EGS capacity.

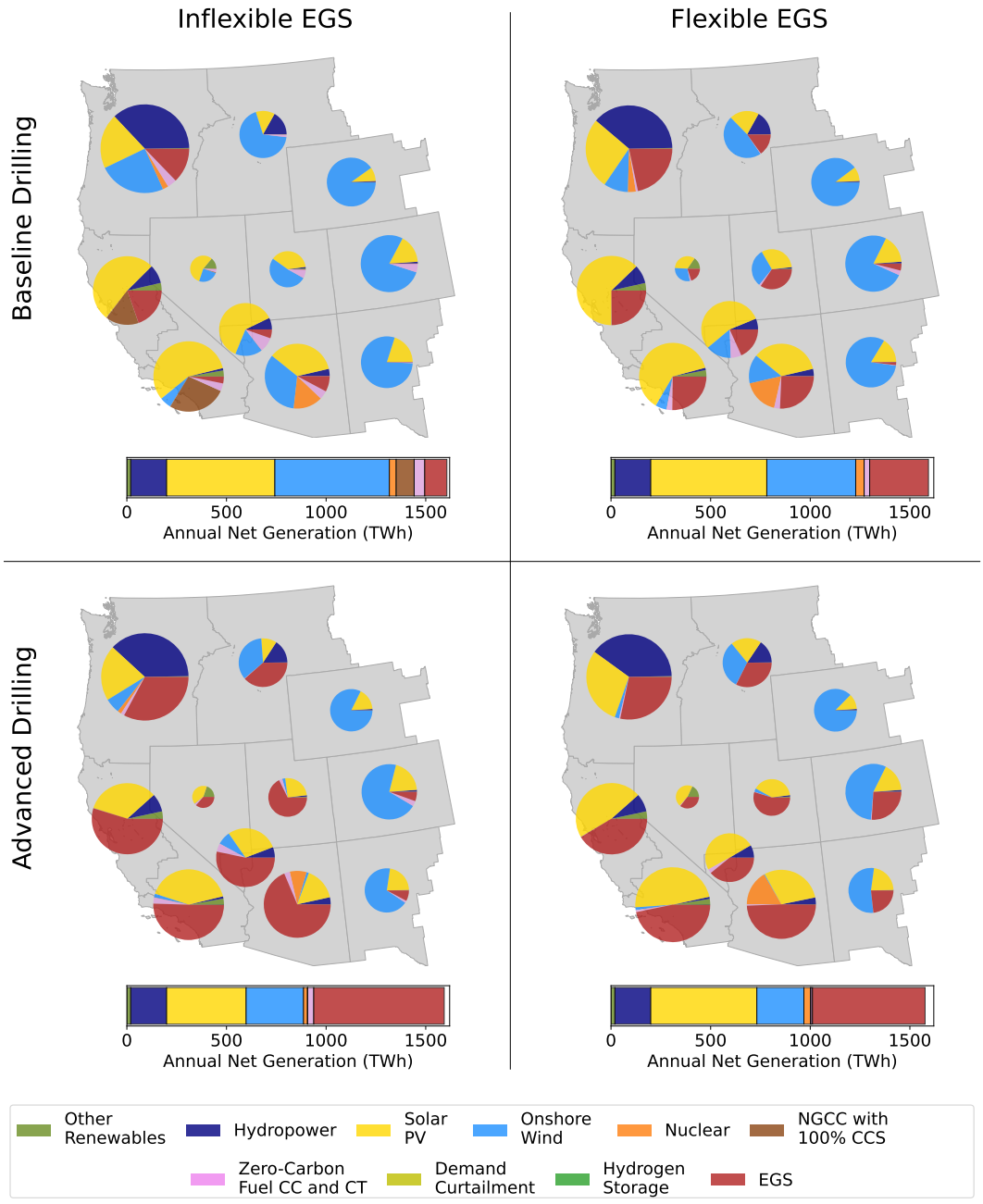

Supplementary Figure 17: Annual generation by technology and model zone for scenarios with mid-case market opportunity and subsurface favorability. Scenarios assuming inflexible and flexible EGS with baseline and advanced drilling are shown. Generation scales with pie chart area.

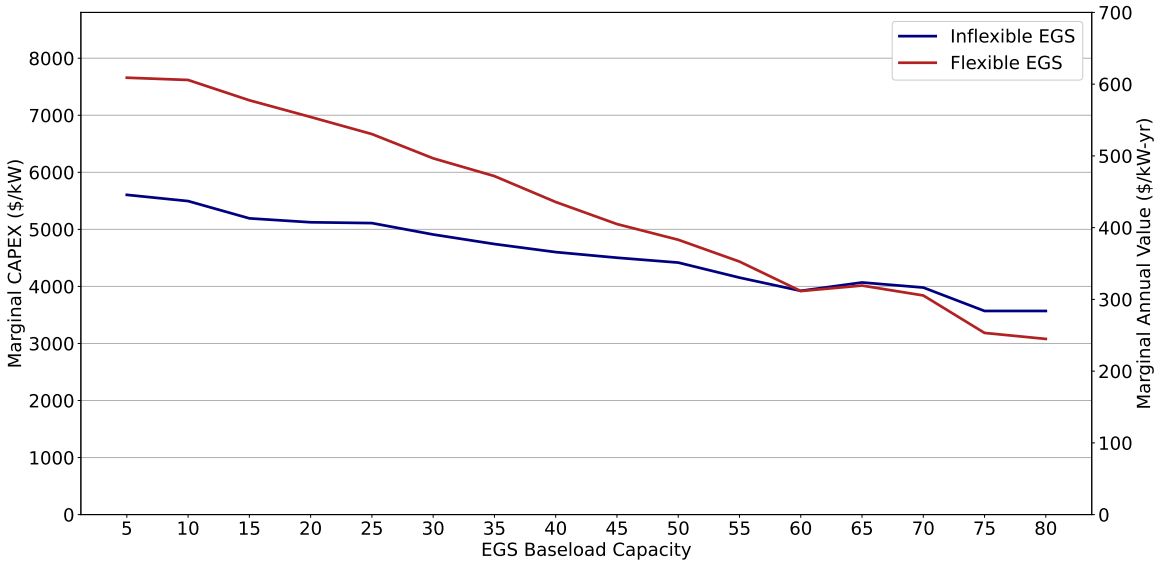

Supplementary Figure 18: Estimated marginal system value of EGS as a function of deployment, for the same cases shown in Figure 5 in the main paper. Marginal value is calculated based on the incremental change in total system cost (excluding the cost of baseload EGS, but including costs associated with component oversizing for flexibility) between sequential cases with fixed EGS baseload capacity. Value is reported on both an annualized basis and as an equivalent CAPEX, which is back-calculated using the EGS discount rate and O&M costs assumed in this paper.

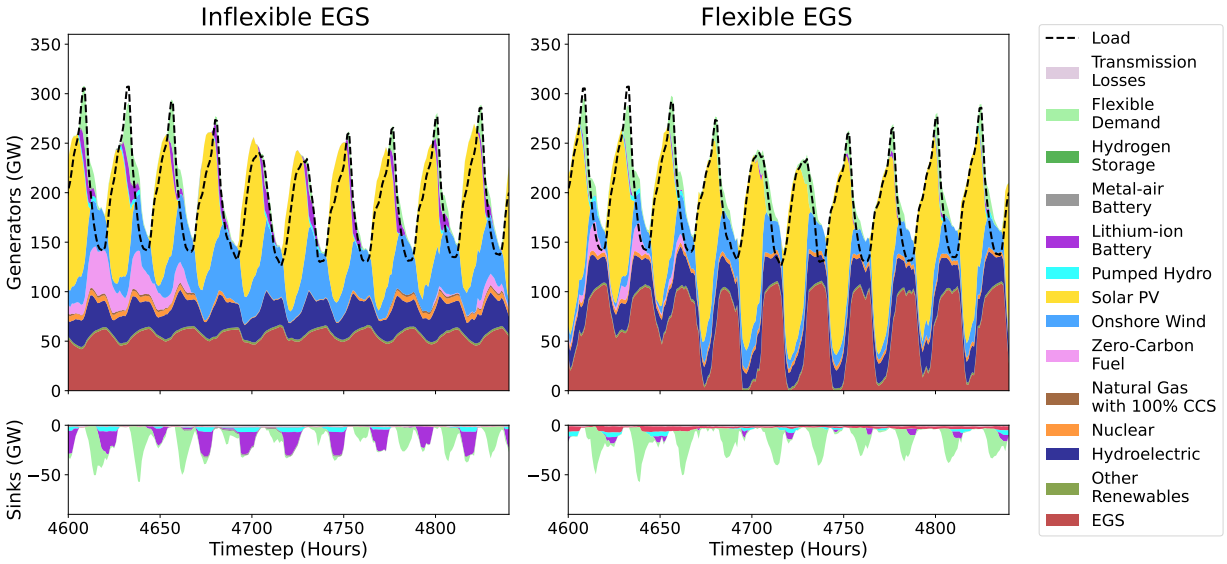

Supplementary Figure 19: Same as Figure 6 in the main paper, for EGS with advanced drilling, with baseload capacity fixed at 70 GW.

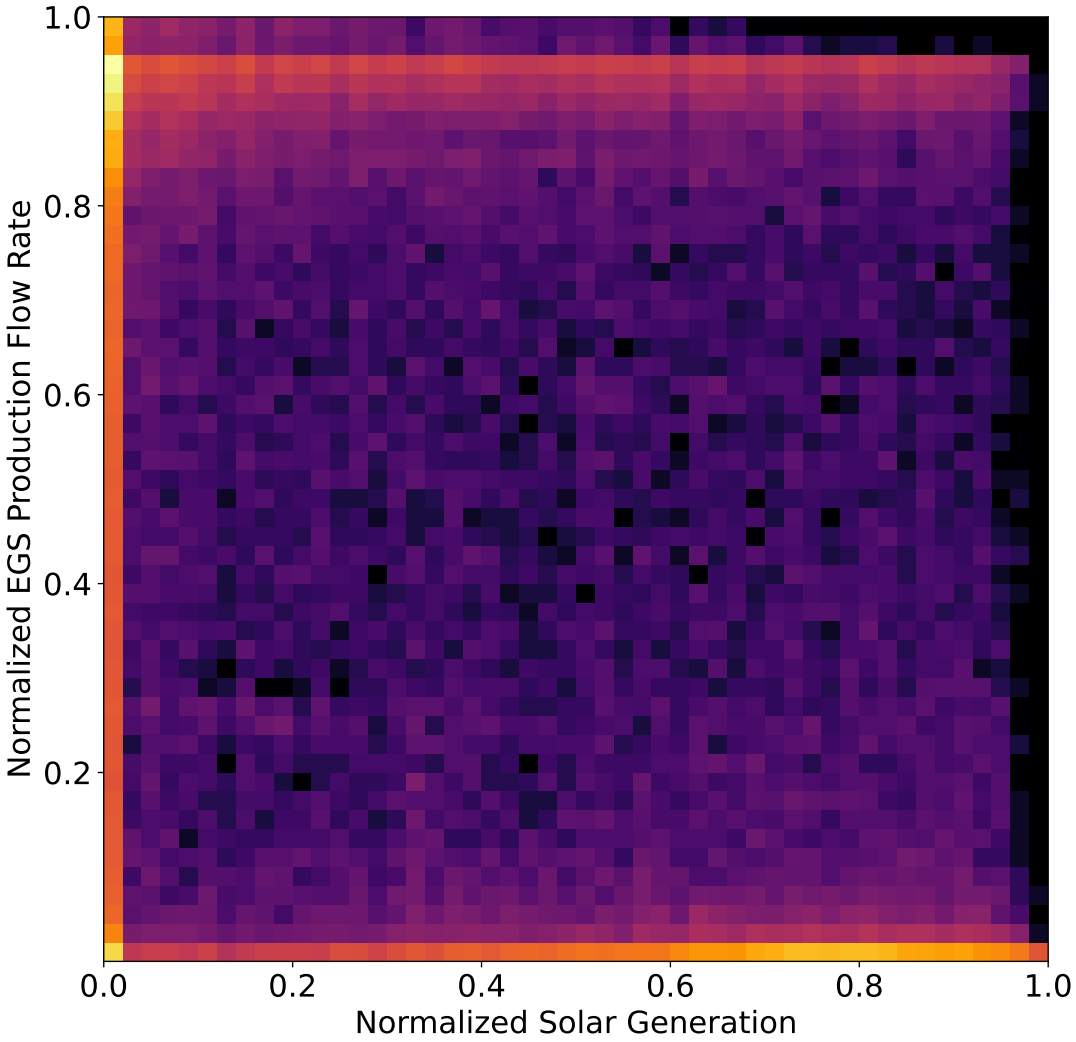

Supplementary Figure 20: Correlation between system-wide aggregate solar generation at each hour of the year and normalized production flow rate from each constructed EGS plant at each hour, for the scenario with baseline geothermal drilling, mid-case market opportunity and subsurface favorability, and EGS flexibility enabled. EGS production rate is typically maximized when solar generation is zero. EGS production is rarely nonzero when solar generation is also nonzero.

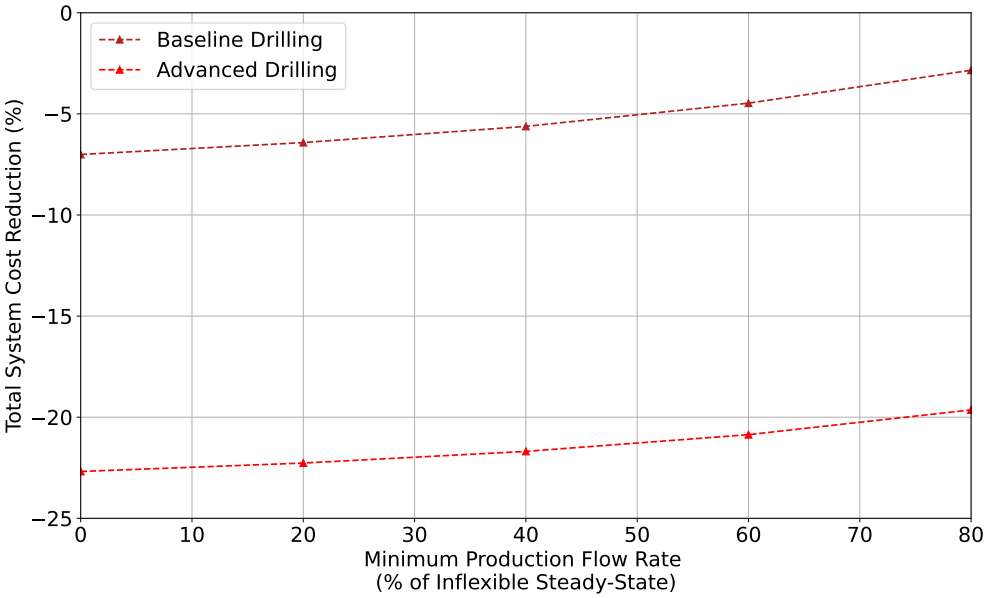

Supplementary Figure 21: Total system cost reduction from EGS deployment as a function of minimum production flow rate for the mid-case market opportunity and subsurface favorability scenario. Increasing the minimum production flow rate reduces the value of flexibility only marginally at first, but the loss of value becomes more severe as the minimum rate is increased further.

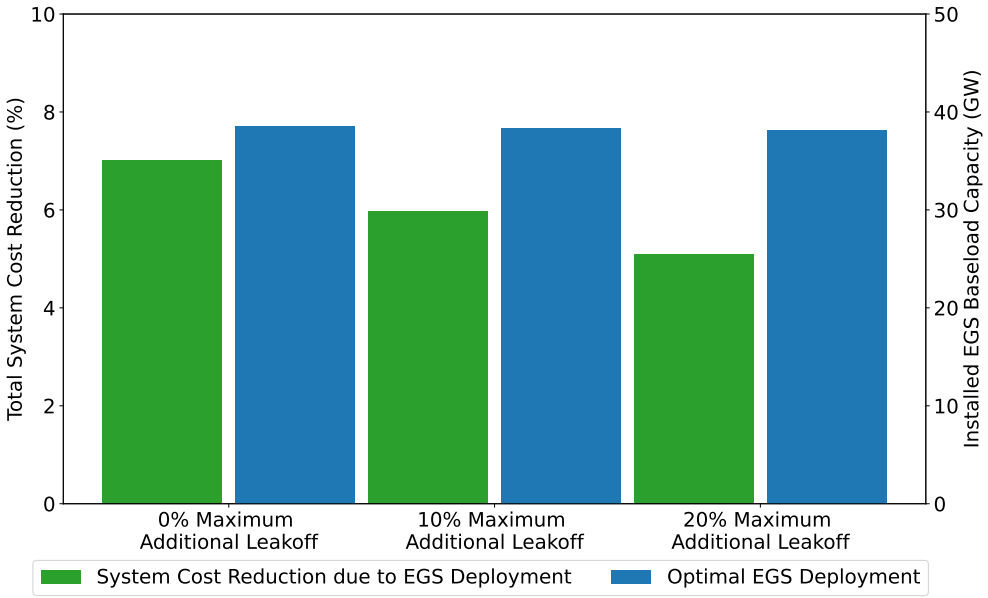

Supplementary Figure 22: Impacts on EGS deployment and total system cost reduction in the case with baseline drilling costs and mid-case market opportunity and subsurface favorability, if increases in subsurface pressure due to flexible operations are assumed to drive additional fluid losses. In these sensitivity cases excess losses are assumed to increase linearly as a function of increasing reservoir pressure beyond the model's steady-state baseline, and the "Maximum Additional Leakoff" is the amount of additional fluid loss (as a percentage of the steady-state injection rate) that is assumed to occur at the maximum allowable reservoir pressure. See Supplementary Note 3.2.3 for a description of the constraint formulation used in these cases.

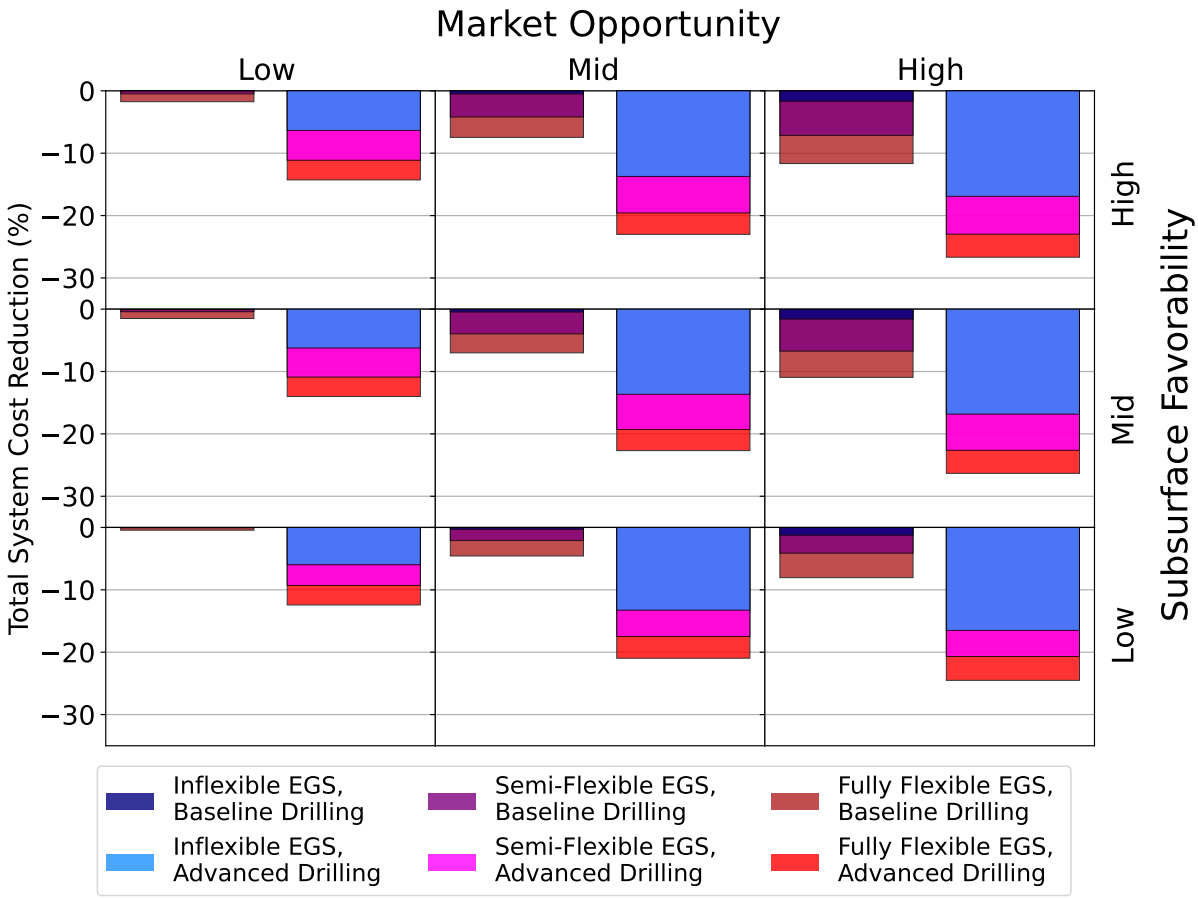

Supplementary Figure 23: System cost reductions from deployment of EGS plants at varying levels of flexibility under a range of scenarios combining EGS market opportunity, subsurface favorability, and drilling cases. Reductions are given with respect to systems with no EGS present. Stacked bars indicate the additional cost reduction from enabling first semi-flexible operations and then fully-flexible operations.

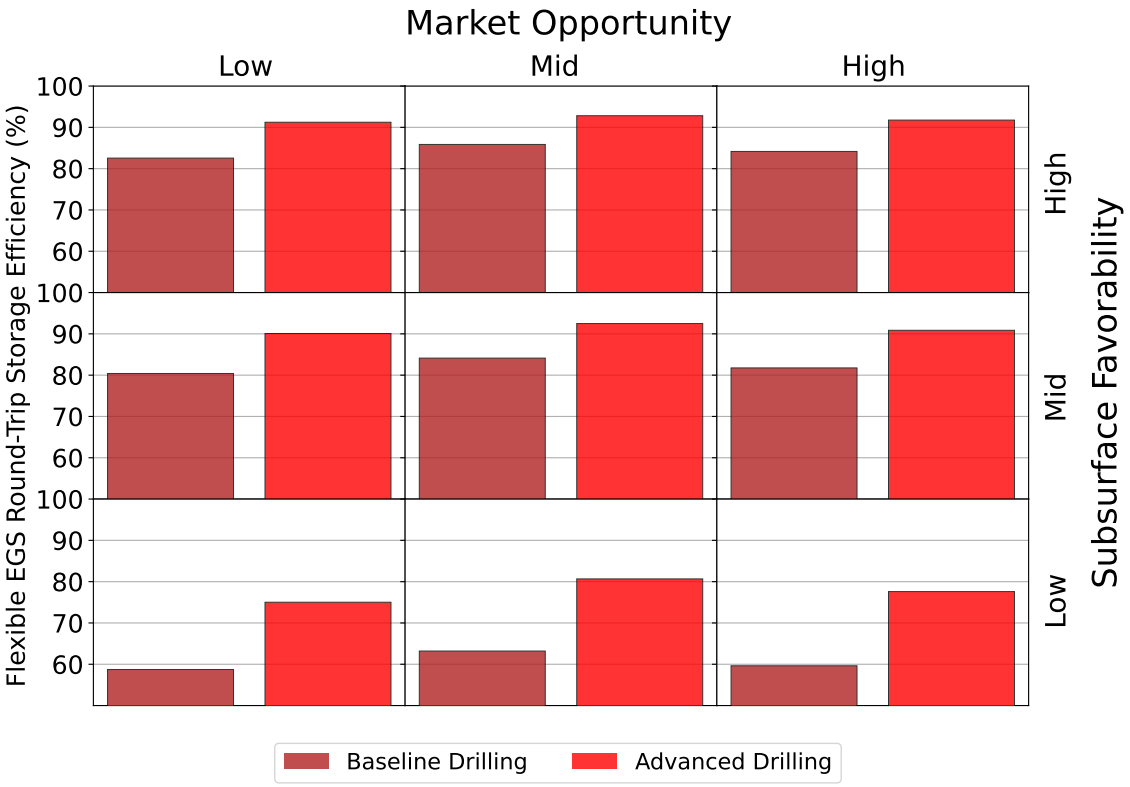

Supplementary Figure 24: Round-trip energy storage efficiencies for flexible EGS plants under a range of scenarios combining EGS market opportunity, subsurface favorability, and drilling cases. Efficiency is calculated as $\eta_{avg} = \left| \frac{\sum_{t\in[1:8760]} \Delta G_t^+}{\sum_{t\in[1:8760]} \Delta G_t^-} \right|$, where $\Delta G_t^{\pm}$ is the deviation of a flexible plant's net generation at hour t from the net generation of an inflexible plant with equal baseload capacity at the same hour, either positive or negative.

Supplementary Note 2: Electricity System Capacity Expansion

This study uses version 0.2.0 of the open-source GenX electricity system capacity expansion model (CEM) [1, 2] to optimize operations and investments for generation, transmission, demand, and storage assets in modeled future electricity systems under a range of scenarios. GenX is modified via a newly-developed 'Geothermal IRES' module, described in detail in Section 3, which captures the operational dynamics of flexible and inflexible enhanced geothermal system (EGS) power plants. The new module will be included in the GenX code base as part of an upcoming release. The current section describes the configuration of GenX for this study and assumptions made with respect to non-EGS resources. All costs are given in 2019 USD. Exact inputs and model settings for each scenario are available at Ricks et al. [3]. All GenX instances are solved in Gurobi, a commercial optimization solver [4], using the barrier solution method and a convergence tolerance of 10^{-4}. This is equivalent to an uncertainty of 0.1% in total system costs, or roughly ±10 MW in optimal capacities by zone.

GenX is configurable to allow for varying levels of model complexity. For this study we run the model at high temporal resolution, optimizing power system operations at hourly resolution over a single weather year. 8760h resolution not only ensures the highest achievable level of accuracy, but is also a requirement of the geothermal IRES module. All generators in the system are bound by basic hourly operational constraints including ramp rates and minimum generation levels. Generation by variable renewable energy (VRE) resources including wind, solar, and run-of-river hydropower is constrained at each timestep based on local weather conditions. Large-scale hydropower resources have fixed hourly inflows and must obey limits on minimum and maximum outflows. State of charge for all storage resources, including reservoir hydro, is calculated based on hourly charge and discharge decisions and constrains total discharge potential. Storage durations are optimized endogenously based on energy and power capacity costs, within exogenously-set minimum and maximum duration limits. In addition to these basic constraints, we also model 'unit commitment' constraints for large thermal resources in this study. These constraints force thermal plants to stay online or offline for minimum durations after startup and shutdown decisions are made, and enforce a minimum generation level when a plant is committed. Startup decisions for thermal plants also incur fixed startup costs and additional fuel use. Although GenX has the capability to model discrete unit commitment decisions using integer variables, we use continuous versions of these constraints in this study. This approach maintains model accuracy in large systems like the ones studied here while drastically improving computation time. Although GenX allows for consideration of operating and contingency reserves, we do not model these in the present study. Inclusion of these constraints leads to much longer run times and has been shown to have a minor effect on optimal capacity and energy mixes [5].

We optimize electricity capacity expansion in the US Western Interconnection using an 11-zone model topology. This topology, shown in Supplementary Figure 25, captures major transmission bottlenecks and differences in demand profiles and resource availability between regions of the western United States. A demand balance constraint is enforced at each model zone, requiring an exact balance of generation, demand, and transmission inflow/outflow. We also include constraints that enforce a capacity reserve planning margin across sets of zones making up subregions of NERC's WECC assessment area [6]. Each region is required to maintain enough dispatchable capacity to meet demand, plus an additional percentage of demand, at all hours of the year. All resources are derated by a fixed factor when calculating their contribution to the system's reserve margin to account for the possibility of outages. NERC subregions and enforced reserve margins are shown in Table 1.

For this study we run GenX myopically over two planning periods, first from 2021 to 2030 and then from 2031 to 2045. Both model runs are 'brownfield' capacity expansions, with the first using the current electricity system as a starting point and the second using the final configuration of the first. This process is repeated for each of the three EGS market opportunity scenarios, as well as for each of

NERC Subregion	GenX Zones	Capacity Reserve Margin
CA/MX	CA_N, CA_S	14%
NWPP-US	ID_MT, PNW, N_NV, UT	16%
RMRG	CO, WY	13%
SRSG	AZ, NM, S_NV	10%

Supplementary Table 1: NERC assessment area subregions, constituent GenX model zones, and enforced capacity reserve planning margins.

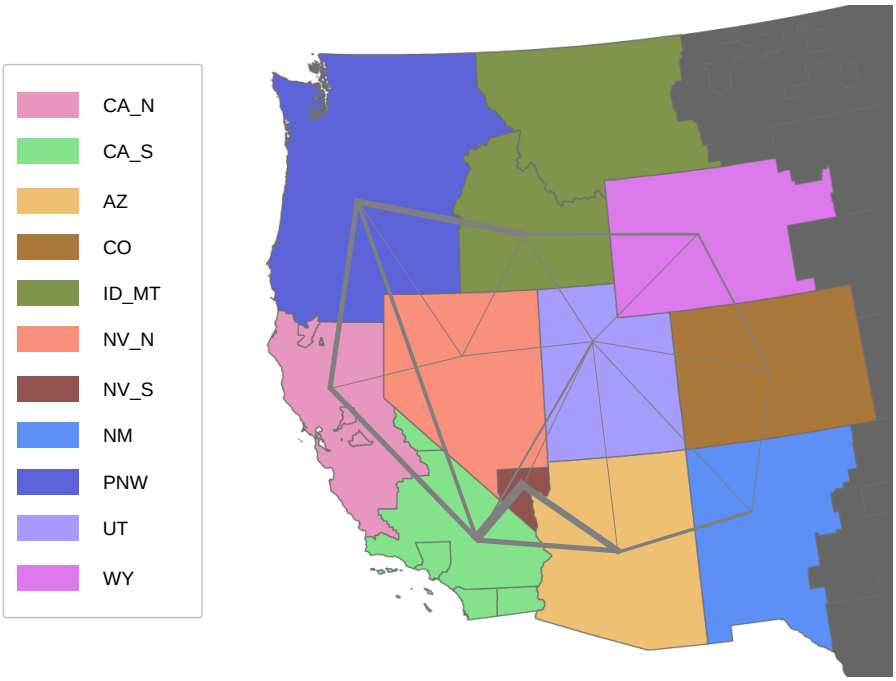

Supplementary Figure 25: 11-zone model topology of the US Western Interconnection, including existing interregional transmission. Aggregations of subregions are shown.

the three decarbonization cases (80%, 90%, and 100% clean), resulting in nine distinct 2045 'baseline' systems representing possible evolutions of the electricity system. During the 2021-2030 planning period EGS deployment is not allowed, and the system is optimized to meet state-mandated renewable or clean energy standards [7]. Where GenX zones contain multiple states, renewable portfolio standards and clean electricity standards acre calculated for the combined zone on a population-weighted basis. In the 2031-2045 planning period we assume a system-wide requirement for carbon-free electricity, both for generation and for the resources available to provide capacity reserves. For scenarios with a full decarbonization mandate, we assume that new natural gas plants from built in the 2021-2030 period can be retrofitted to run on zero-carbon fuels (ZCFs) at zero additional cost, but that legacy gas and coal plants built before this period must be retired. In these cases, all gas plants without post-combustion capture are assumed to run on ZCFs in 2045. For cases without a full decarbonization mandate, existing coal and gas plants are allowed to remain in operation, and all new gas plants are assumed to run on natural gas rather than ZCFs. In all cases, the only relevant remaining state policy in 2045 is a moratorium on new nuclear construction in the state of California.

Zonal load profiles, cost and performance inputs for existing and new-build technologies, and existing transmission topologies are all compiled using PowerGenome, an open-source software described in detail elsewhere [8]. Electricity load profiles are created in the 'efs_demand' branch of PowerGenome, and assume significant electrification of end-use demand across the economy, in line with national decarbonization goals. Baseline load profiles are derived from historical data for the 2012 weather year, and are scaled up for the 2030 or 2045 planning years assuming a constant annual growth factor. Total stocks of additional electrified demand across various economic sectors are sourced for the 2030 and 2045 planning years from results for the high-electrification 'E+' scenario from Larson et al. [9]. Hourly load profiles for the 2012 weather year in each demand category are taken from Mai et al. [10] and added to the baseline load profiles to create a final profile. The final system-wide hourly load profile for the 2045 planning year is shown in Supplementary Figure 26. Given the highly flexible nature of some electrified end uses, we include flexibility options for several categories of electrified demand following methodology used in Mai et al. [10]. We assume that light-duty vehicle charging demand can be delayed up to five hours, and that residential water heating demand can be advanced up to two hours or delayed up to two hours. The level of demand flexibility varies depending on the EGS market opportunity scenario. We assume that 90/75/60% of EV charging and 20/10/0% of residential water heating demand are flexible across the low/mid/high market opportunity scenarios.

We use the master branch of PowerGenome to compile all input data except load and flexible demand.

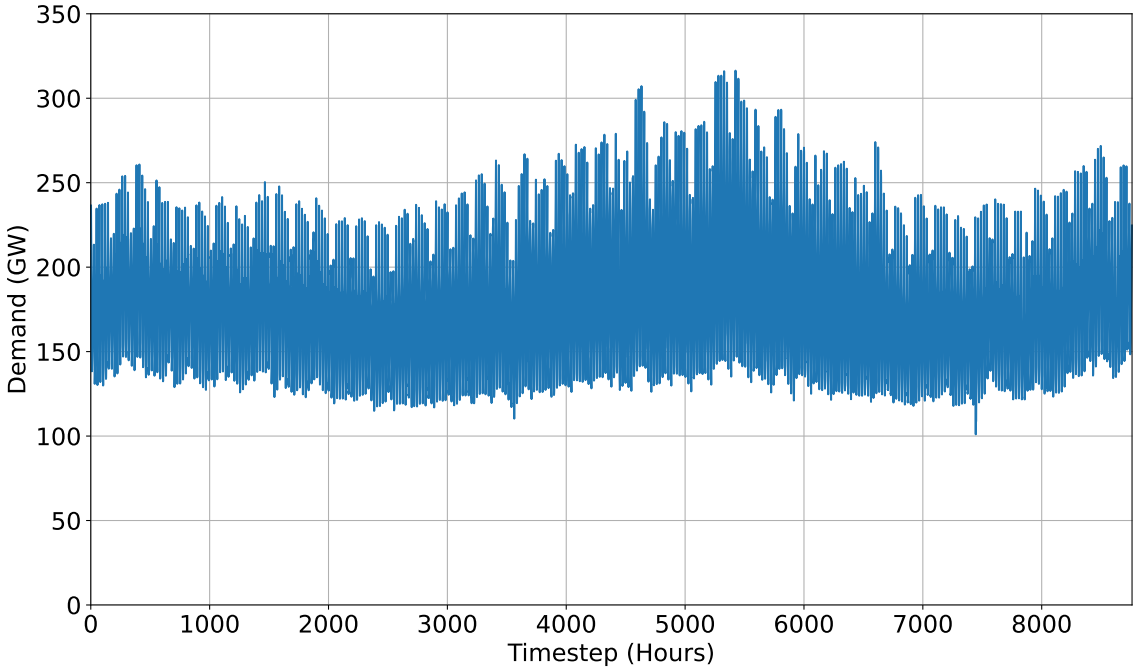

Supplementary Figure 26: System-wide hourly load profile for the Western Interconnection in 2045, including electrification.

Existing utility-scale generation, storage, and transmission capacities and performance characteristics are collected from the Public Utility Data Liberation (PUDL) project database [11]. Existing generators are clustered by technology using a k-means process, resulting in 1-2 clusters per technology per zone. Hydropower reservoirs in the western US are assumed to have a storage capacity equal to four times the average annual reservoir inflow, and pumped hydro facilities are assumed to have storage durations of 15.5 hours [12]. Existing distributed solar capacities are gathered by state from the Energy Information Administration (EIA) for 861M [13]. States with mandated distributed generation targets as a percentage of total load, including Arizona and Colorado, have capacities calculated directly based on these requirements [7]. Distributed solar profiles for the largest urban area in each GenX zone are downloaded from Renewables Ninja [14], and assume fixed-angle panels with 10% losses.

Cost and performance data for newly-built technologies are primarily taken from the National Renewable Energy Laboratory's Annual Technology Baseline (NREL ATB), 2021 edition [15]. These include project CAPEX, weighted-average cost of capital (WACC), fixed and variable O&M costs, and heat rate. Parameters for each GenX model period are taken as the average of ATB parameters across that period. All average cost and performance assumptions for newly-built technologies in the 2031-2045 planning period are shown in Tables 2 and 2. Capital costs for all technologies are modified by regional multipliers taken from the EIA's Annual Energy Outlook (AEO) [16] to account for regional differences in construction costs.

Resource	Power CAPEX ($/kW)	Energy CAPEX ($/kWh)	Real WACC	Lifetime (yrs)	Spur Length (km)	Power Fixed O&M ($/kW-yr)	Energy Fixed O&M ($/kWh-yr)	Variable O&M ($/MWhr)	Fuel	Heat Rate (GJ/MW)
Utility PV	575/721/721	N/A	2.57	30	Variable	13.9/16.0/16.0	N/A	0	N/A	N/A
Onshore Wind	630/874/874	N/A	3.00	30	Variable	30.3/36.6/36.6	N/A	0	N/A	N/A
Offshore Wind	4378/4476/4476	N/A	3.21	30	Variable	66.6/75.4/75.4	N/A	0	N/A	N/A
Lithium-Ion Battery	91/191/191	97/129/129	2.57[a]	15	16.1	2.3/4.8/4.8	2.4/3.2/3.2	0.15	N/A	N/A
Metal-Air Battery	800/1200/2000	8/12/20	2.57[a]	25	16.1	20.0/30.0/50.0	0.2/0.3/0.5	0	N/A	N/A
H_2 Storage (Charge)	300/450/675	2/5/10	2.57[a]	25	0	7.5/11.3/16.9	0.05/0.125/0.250	0	N/A	N/A
Nuclear	4311/6468/9702	N/A	3.34	40	80.5	145.0	N/A	2.35	Uranium	11.04
NGCC + 100% CCS	2419	N/A	3.34	30	32.2	78.4	N/A	6.2	Natural Gas	7.93
ZCF CC	964	N/A	3.34	30	32.2	27.3	N/A	1.7	ZCF	6.71
ZCF CT	810	N/A	3.34	30	32.2	20.9	N/A	4.9	ZCF	10.25

Supplementary Table 2: New-build technology cost and performance assumptions (before regional adjustments) for (Low/Mid/High) Market Opportunity cases in the 2031-2045 buildout period. Hydrogen storage has different charge and discharge power capacity parameters. Charge parameters for electrolysis are shown, and discharge cost parameters are identical to those of ZCF CTs. [a]Missing from NREL ATB, set equal to solar.

Resource	Start Cost ($/MW)	Start Fuel (GJ/MW)	Up Time (hrs)	Down Time (hrs)	Ramp Rate (%/hr)	Min Power (%)	Charge Efficiency (%)	Discharge Efficiency (%)	Min Duration (hrs)	Max Duration (hrs)	Capacity Reserve Contribution (%)
Utility PV	N/A	N/A	N/A	N/A	100	N/A	N/A	N/A	N/A	N/A	80
Onshore Wind	N/A	N/A	N/A	N/A	100	N/A	N/A	N/A	N/A	N/A	80
Offshore Wind	N/A	N/A	N/A	N/A	100	N/A	N/A	N/A	N/A	N/A	80
Lithium-Ion Battery	N/A	N/A	N/A	N/A	100	N/A	92	92	1	10	95
Metal-Air Battery	N/A	N/A	N/A	N/A	100	N/A	75	36	1	1000	95
H_2 Storage (Charge)	N/A	N/A	N/A	N/A	100	N/A	65	65	1	300	95
Nuclear	278	N/A	24	24	25	50	N/A	N/A	N/A	N/A	90
NGCC + 100% CCS	103	2.11	6	6	64	60	N/A	N/A	N/A	N/A	90
ZCF CC	103	2.11	6	6	64	20	N/A	N/A	N/A	N/A	90
ZCF CT	134	3.69	1	1	100	30	N/A	N/A	N/A	N/A	90

Supplementary Table 3: Additional new-build technology performance assumptions.

Technology costs in the mid-case EGS market opportunity scenario generally follow the 'Moderate' cost assumptions from the ATB. Exceptions are metal-air batteries and hydrogen storage, which are not listed in the ATB and for which we use cost and performance assumptions adapted from Baik et al. [17] and Viswanathan et al. [18], respectively, and natural gas combined cycle plants with carbon capture and storage (NGCC/CCS). Because only the 'Conservative' cost and performance assumptions for natural gas plants with CCS in the ATB assume a conventional combined cycle plant (rather than a fuel cell or an interpolation between the two), we use the conservative case as our baseline for this category of plant. NGCC/CCS cost and performance parameters are adjusted further to reflect the requirement of 100% carbon capture efficiency in our system, an increase from the 90% efficiency assumed in the ATB. Capital cost is increased by \$116/kW, heat rate by 0.365, fixed O&M by \$9.67/kW-yr, and variable O&M by 7.6%. We further consider the need for CO_2 transport and storage infrastructure, the cost of which varies by model zone. CO_2 pipeline construction costs are added to NGCC/CCS plant investment costs, and are calculated using methodology developed in Larson et al. [9], assuming an average plant size of 500 MW, a 100% utilization rate, and a length equal to the distance between the largest major metro area in each GenX zone and the edge of the nearest CO_2 injection basin. Variable injection costs per ton of CO_2 are added to NGCC/CCS plant variable operational costs, and vary by injection basin. CO_2 pipeline costs by GenX zone are listed in Table 4. Large pipeline costs make NGCC/CCS an uneconomic resource in some model zones. Fuel costs for natural gas and uranium in the mid-case market opportunity scenario in each GenX planning year are taken from reference case in the EIA AEO 2021, and vary by region [19]. The cost of ZCFs in the 2045 planning year is assumed to be constant in all zones, and is set equal to the average cost of hydrogen in the year 2050 across the three high-electrification scenarios in Larson et al. [9].

For low and high EGS market opportinity scenarios, costs of non-EGS technologies are generally lower and higher, respectively. Wind, solar, and lithium-ion battery costs follow the 'Advanced' ATB cost case in our low market opportunity case. Their costs still follow the 'Moderate' ATB cost case in our high market opportunity case, as we consider the 'Conservative' ATB cost case for these resources to be highly unlikely. For new nuclear resources, which only have a single cost case in the ATB, we assume that capital costs are 33% lower in the low market opportunity case and 50% higher in the high market opportunity case. For metal-air storage, we assume the same -33%/+50% multipliers for all cost components in the low/high market opportunity cases. For hydrogen storage, we vary electrolyzer costs by -33%/+50% around a \$450/kW mid-case, and geologic storage costs from \$2/kWh to \$5/kWh to \$10/kWh in the low/mid/high cases to reflect the range of costs referenced in Viswanathan et al. [18]. Hydrogen storage discharge is assumed to use combustion turbines, which do not vary in cost between cases. As variable costs are the largest component of levelized cost of energy (LCOE) for NGCC/CCS and ZCF plants, we vary these rather than fixed costs in the low/high market opportunity cases. Low/high fuel costs for natural gas follow the low and high oil and gas resource scenarios in EIA [19], and low/high costs for ZCFs assume -33%/+50% compared to the mid-case. Fuel costs in all scenarios in all zones are given in Table .

Transmission interconnection costs are considered separately for all newly-built resources. For non-VRE resources, costs are calculated based on an assumed spur line length and regional spur line cost. Regional spur line costs are adopted from NREL's ReEDS CEM [20], and are assumed to be \$9241/MW-mile in the CA_N and CA_S zones and \$4107/MW-mile elsewhere. Spur line distances are assumed to be 20 miles for natural gas plants, 50 miles for nuclear plants, and 10 miles for storage. Grid interconnection costs for VREs and inter-zonal transmission expansion costs are calculated using a cost-surface method developed in Larson et al. [9]. All transmission capital costs are converted to annuities assuming a 4.2% real WACC and a 60 year payback period.

Finally, generation profiles for existing and new-build wind and solar resources are aggregated in PowerGenome using historical data for the 2012 weather year. Hourly capacity factor time series and project interconnection costs (for new-build resources) are calculated at 16 km $\times$ 16 km spatial resolution for both wind and solar resources. Profiles include factors such as resource degradation, inverter loading ratios, losses from DC/AC conversion. Existing resources are grouped into single clusters by GenX zone and generation profiles are averaged across all generators, with weighting by capacity. New-build resources are organized into a user-determined number of clusters in each zone, typically 4-8, with resources sorted by LCOE using a k-means clustering method. Generation profiles and interconnection costs are calculated for these clusters using a capacity-weighted approach.

All PowerGenome and GenX input files and raw results related to this work are available in Ricks et al. [3].

GenX Zone	Annuity ($/MW)	Variable O&M ($/MWh)
CA_N	6952	4.87
CA_S	16908	4.87
AZ	85759	4.87
CO	21265	6.20
ID_MT	77427	4.87
NV_N	20179	4.87
NV_S	46962	4.87
NM	46962	16.65
PNW	114736	4.87
UT	94065	6.20
WY	5825	9.13

Supplementary Table 4: CO_2 pipeline and injection cost adders for NGCC/CCS plants by GenX zone.

EGS Market Opportunity	Pacific Gas	Pacific Uranium	Rockies Gas	Rockies Uranium	ZCF
Low	3.23	0.76	3.45	0.76	10.14
Mid	4.31	0.76	4.58	0.76	15.20
High	7.31	0.76	7.71	0.76	22.81

Supplementary Table 5: Fuel cost assumptions under three EGS market opportunity scenarios. Non-ZCF fuel costs are projections from the EIA Annual Energy Outlook [19]. The Pacific fuel region includes the CA_N, CA_S, and PNW model zones. The Rockies fuel region contains all other model zones. Mid-case ZCF fuel cost is equal to the average cost of hydrogen in 2045 in three high-electrification scenarios from Larson et al. [9]. Low/high-case ZCF costs are -33%/+50% the mid-case cost.

Supplementary Note 3: Modeling Flexible Geothermal Power

In-reservoir energy storage (IRES) at EGS power plants could plausibly be modeled in the same manner as other storage technologies in GenX, assigning it an hourly state of charge variable as well as energy and power capacities. However, doing so would abstract many of the critical dynamics of flexibly-operated EGS reservoirs and lead to significant inaccuracies. Unlike in traditional storage technologies, the change in pressure in an EGS reservoir at a moment in time depends not only on the injection and projection well flow rates at that same moment, but also on the entire recent history of flow rates. Maximum discharge for flexible EGS plants is constrained not only by power plant capacity, but also by the current reservoir pressure. Furthermore, there is a nonlinear relationship between injection flow rate and the parasitic load from injection pumping. We have therefore developed a new module for GenX explicitly designed to model flexible wellfield operations and IRES at EGS power plants. This model formulation was first developed and validated in Ricks et al. [21], and was shown to be capable of accurately reproducing the pressure and flow behaviors observed in numerical reservoir simulations. The following subsections describe the formulation of this module and its implementation within the larger GenX framework. Values and bounds for pressure and flow variables are given in terms of baseline values corresponding to a single EGS injection well, which are then scaled based on the installed baseload capacity for each EGS resource cluster in GenX. Note that following the unit conventions of the reservoir simulation software used in this study, geofluid mass flow rates in the model formulation are given in units of STB/min, and pressures in psi. The exception to this convention is surface geofluid storage tank volume, which as a direct model input/output is given in liters.

Supplementary Note 3.0.1: Geothermal IRES module indices, variables, expressions, and parameters

Supplementary Table 6: Model Indices

Notation	Description
$t \in T$	Where t denotes an hour in the modeled weather year.
$u \in U$	Where u denotes an hour in the modeled weather year. The set U contains an additional 360 timesteps compared to the set T, and t is equivalent to $u - 360$.
$c \in C$	Where C is the set of all geothermal generators to which IRES constraints apply.
$z \in Z$	Where Z is the set of all model zones.
$r \in R$	Where R is the set of capacity reserve margin constraints.

Supplementary Table 7: New Model Variables and Expressions

Notation	Description
y_c^{BASE}	Installed baseload generating capacity for resource cluster c.
y_c^{FLEX}	Installed flexible surface generator capacity (above baseload) for resource cluster c.
y_c^{PUMP}	Installed injection pumping power capacity for resource cluster c.
y_c^{TANK}	Installed surface geofluid storage capacity for resource cluster c.
y_c^{IC}	Grid interconnection capacity for resource cluster c.
$x_{c,t}^{P\_IRES}$	Net electric power (not including injection pumping load) generated by resource cluster c at hour t.
$x_{c,t}^{MAXP\_IRES}$	Maximum possible net electric power (not including injection pumping load) generated by resource cluster c at hour t.
$x_{c,t}^{PP\_IRES}$	Injection pumping load for resource cluster c at hour t.
$x_{c,t}^{GFM}$	Makeup water imported at hour t, for resource cluster c.
$x_{c,t}^{GFS}$	Amount of geofluid in surface storage at hour t, for resource cluster c.
$x_{c,u}^{PROD}$	Geofluid production mass flow rate for resource cluster c at timestep u.
$x_{c,u}^{MAXPROD}$	Maximum possible geofluid production mass flow rate for resource cluster c at timestep u.
$x_{c,u}^{PUP1}$	First segment of positive deviation from the steady-state fluid injection rate for resource cluster c at timestep u.
$x_{c,u}^{PUP2}$	Second segment of positive deviation from the steady-state fluid injection rate for resource cluster c at timestep u.
$x_{c,u}^{PUP3}$	Third segment of positive deviation from the steady-state fluid injection rate for resource cluster c at timestep u.
$x_{c,u}^{PDN1}$	First segment of negative deviation from the steady-state fluid injection rate for resource cluster c at timestep u.
$x_{c,u}^{PDN2}$	Second segment of negative deviation from the steady-state fluid injection rate for resource cluster c at timestep u.
$x_{c,u}^{PDN3}$	Third segment of negative deviation from the steady-state fluid injection rate for resource cluster c at timestep u.
$x_{c,u}^{INJSQ}$	Square of the geofluid injection mass flow rate for resource cluster c at timestep u.
$x_{c,u}^{IPRESSURE}$	Injection well bottomhole pressure for resource cluster c at timestep u.
$x_{c,u}^{PPRESSURE}$	Production well bottomhole pressure for resource cluster c at timestep u.
$e_{c,t}^{IRES\_NoVar}$	Net electric power (not including injection pumping load) that would be generated by resource cluster c at hour t if the capacity factor at hour t were 1.
$e_{c,t}^{IRES\_MaxNoVar}$	Maximum possible net electric power (not including injection pumping load) that could be generated by resource cluster c at hour t if the capacity factor at hour t were 1.
$e_{c,t}^{IRES\_Net}$	Net electric power (including injection pumping load) generated by resource cluster c at hour t.
$e_{c,u}^{INJ}$	Geofluid injection mass flow rate for resource cluster c at timestep u.
$e_{c,t}^{IRES\_PumpPower}$	Expression for the net required injection pumping power for resource cluster c at hour t.
$e_{c,u}^{Leakoff\_Inj}$	Subsurface fluid loss due to excess injection bottomhole pressure for resource cluster c at hour u.
$e_{c,u}^{Leakoff\_Prod}$	Subsurface fluid loss due to excess production bottomhole pressure for resource cluster c at hour u.

Supplementary Table 8: New Model Variables and Expressions

Notation	Description
p_c^{Cap}	Baseload net electric generating capacity (excluding injection pumping load) per injection well for resource cluster c.
p_c^{MaxCap}	Maximum deployable baseload capacity for resource cluster c.
$p_{c,r}^{CapRes}$	Multiplier determining the contribution of resource cluster c to capacity reserve margin constraint r.
$p_c^{Hydrostatic}$	Injection well hydrostatic pressure for resource cluster c.
$p_c^{MaxIPressure}$	Maximum allowed injection well bottomhole pressure for resource cluster c.
$p_c^{MinIPressure}$	Minimum allowed injection well bottomhole pressure for resource cluster c.
$p_c^{MinPPressure}$	Minimum allowed production well bottomhole pressure for resource cluster c.
$p_c^{WellPres0}$	Injection wellhead pressure when injection well bottomhole pressure is equal to $p_c^{MinIPressure}$ and injection flow rate is 0, for resource cluster c.
$p_c^{WellPres1}$	Additional injection wellhead pressure due to friction from pumping at 1/3 the steady-state injection rate, for resource cluster c.
$p_c^{WellPres2}$	Additional injection wellhead pressure due to friction from pumping at 2/3 the steady-state injection rate, for resource cluster c.
$p_c^{WellPres3}$	Additional injection wellhead pressure due to friction from pumping at the steady-state injection rate, for resource cluster c.
$p_c^{WellPres4}$	Additional injection wellhead pressure due to friction from pumping at 4/3 the steady-state injection rate, for resource cluster c.
$p_c^{WellPres5}$	Additional injection wellhead pressure due to friction from pumping at 5/3 the steady-state injection rate, for resource cluster c.
$p_c^{WellPres6}$	Additional injection wellhead pressure due to friction from pumping at double the steady-state injection rate, for resource cluster c.
p_c^{M}	Slope of the linear relationship between production well bottomhole pressure and maximum achievable production flow rate, for resource cluster c.
p_c^{B}	Intercept of the linear relationship between production well bottomhole pressure and maximum achievable production flow rate, for resource cluster c.
$p_{c,[0:50]}^{pp}$	Hourly coefficients of the transient production well bottomhole pressure response function corresponding to changes in production flow rate, for resource cluster c.
$p_{c,[1:50]}^{ip}$	Hourly coefficients of the transient production well bottomhole pressure response function corresponding to changes in injection flow rate, for resource cluster c.
$p_{c,[1:50]}^{pi}$	Hourly coefficients of the transient injection well bottomhole pressure response function corresponding to changes in production flow rate, for resource cluster c.
$p_{c,[0:50]}^{ii}$	Hourly coefficients of the transient injection well bottomhole pressure response function corresponding to changes in injection flow rate, for resource cluster c.
p_c^{ss}	Constant pressure response rate for all wells after 50 timesteps, for resource cluster c.
p^{IPF}	Conversion factor used to translate injection rate and wellhead pressure into a required electric pumping power.
$p_c^{BaseProd}$	Steady-state production flow rate for resource cluster c.
$p_c^{MinProdFrac}$	Multiplier for setting the minimum allowable production flow rate, for resource cluster c.
$p^{MaxLeakoff}$	Multiplier determining the maximum subsurface fluid loss rate due to elevated reservoir pressure.
$p_{c,t}^{IresVar}$	Capacity factor multiplier corresponding to the generating efficiency of resource cluster c based on ambient conditions at hour t.
$p_c^{BaseCost}$	Annual fixed costs per MW of baseload capacity for resource cluster c.
$p_c^{FlexCost}$	Annual fixed costs per MW of flexible generator capacity for resource cluster c.
$p_c^{PumpCost}$	Annual fixed costs per MW of injection pump power capacity for resource cluster c.
p_c^{ICCost}	Annual fixed costs per MW of grid interconnection capacity for resource cluster c.
$p_c^{TankCost}$	Annual fixed costs per million liters of surface geofluid storage capacity for resource cluster c.

Supplementary Note 3.1: Objective Function Contribution

The GenX Objective Function minimizes total annual electricity system fixed and variable costs. Geothermal IRES generators have no variable cost, and so contribute only fixed costs to this total. The total cost contributed to the objective function is given in equation (1). Each term sums the total cost contribution from each plant component across all resource clusters $c \in C$.

$$e^{TotalCIRES} = \sum_{c \in C} \Big(y_c^{BASE} \cdot p_c^{BaseCost} + y_c^{FLEX} \cdot p_c^{FlexCost} + \tag{1a}$$

$$y_c^{PUMP} \cdot p_c^{PumpCost} + y_c^{IC} \cdot p_c^{ICCost} + y_c^{TANK} \cdot p_c^{TankCost} \Big) \tag{1b}$$

Supplementary Note 3.2: Constraints

The geothermal IRES formulation consists of a set of constraints that define the feasible solution space for the decision variables. Geothermal IRES module decision variables are also included in existing GenX constraints. The net generation from each EGS generator cluster c at hour t, $e_{c,t}^{IRES\_Net}$, is added to the main demand balance constraint for the generator's respective GenX model zone. Net generation is also used to quantify each EGS generator's contribution to the system's local capacity reserve margin constraint, where it is multiplied by a derating factor of 0.9 in line with other thermal resources.

Supplementary Note 3.2.1: Variable Bounds

These constraints establish hard bounds on the decision variables of the optimization problem. Some variables are only bounded on one end.

$$p_c^{MaxCap} \geq y_c^{BASE} \geq 0 \qquad \forall c \in C \tag{2a}$$
$$y_c^{FLEX} \geq 0 \qquad \forall c \in C \tag{2b}$$
$$y_c^{PUMP} \geq 0 \qquad \forall c \in C \tag{2c}$$
$$y_c^{TANK} \geq 0 \qquad \forall c \in C \tag{2d}$$
$$y_c^{IC} \geq 0 \qquad \forall c \in C \tag{2e}$$
$$x_{c,t}^{P\_IRES} \geq 0 \qquad \forall c \in C, t \in T \tag{2f}$$
$$x_{c,t}^{MAXP\_IRES} \geq 0 \qquad \forall c \in C, t \in T \tag{2g}$$
$$x_{c,t}^{PP\_IRES} \geq 0 \qquad \forall c \in C, t \in T \tag{2h}$$
$$x_{c,t}^{GFM} \geq 0 \qquad \forall c \in C, t \in T \tag{2i}$$
$$x_{c,t}^{GFS} \geq 0 \qquad \forall c \in C, t \in T \tag{2j}$$
$$x_{c,u}^{PROD} \geq 0 \qquad \forall c \in C, u \in U \tag{2k}$$
$$x_{c,t}^{MAXPROD} \geq 0 \qquad \forall c \in C, t \in T \tag{2l}$$
$$x_{c,u}^{PUP1} \geq 0 \qquad \forall c \in C, u \in U \tag{2m}$$
$$x_{c,u}^{PUP2} \geq 0 \qquad \forall c \in C, u \in U \tag{2n}$$
$$x_{c,u}^{PUP3} \geq 0 \qquad \forall c \in C, u \in U \tag{2o}$$
$$x_{c,u}^{PUP4} \geq 0 \qquad \forall c \in C, u \in U \tag{2p}$$
$$x_{c,u}^{PUP5} \geq 0 \qquad \forall c \in C, u \in U \tag{2q}$$
$$x_{c,u}^{PUP6} \geq 0 \qquad \forall c \in C, u \in U \tag{2r}$$
$$x_{c,u}^{INJSQ} \geq 0 \qquad \forall c \in C, u \in U \tag{2s}$$
$$p_c^{MaxIPressure} \geq x_{c,u}^{IPRESSURE} \geq p_c^{MinIPressure} \qquad \forall c \in C, u \in U \tag{2t}$$
$$x_{c,u}^{PPRESSURE} \geq p_c^{MinPPressure} \qquad \forall c \in C, u \in U \tag{2u}$$

All new variables are constrained to be greater than or equal to 0. Eq. (2a) constrains the installed baseload capacity for a resource cluster to be less than or equal to the maximum resource potential of that cluster. Eq. (2t) constrains the injection well bottomhole pressure to always be greater than or

equal to its minimum allowable value, which is also its steady-state value, and less than or equal to its maximum allowable value. For this work we fix the maximum injection pressure at 2 MPa higher than the minimum injection pressure. We do so to reflect the need to avoid large pressure fluctuations that damage reservoir integrity or induce seismicity. Although this value is lower than the 3.5 MPa increase allowed in Ricks et al. [21], it was found in that work that reducing the maximum allowable pressure did not significantly reduce the value of IRES. Given the absence of data on the risks of elevated reservoir pressures, we adopt the more conservative value in this work. Eq. (2u) constrains production well bottomhole pressure to be always greater than or equal to its minimum allowable value, which is also its steady-state value. Requiring bottomhole pressures to remain above their steady-state values lowers the risk of fracture closure.

Supplementary Note 3.2.2: Initial Conditions

Most of the state variables in the geothermal IRES model are formulated in a manner that references previous states. The initial conditions set for all operational variables at timestep $u = 1$ represent the status of a plant in steady-state (i.e. inflexible) operation, and are fixed with respect to the installed baseload capacity. All operational decision variables are held at their initial conditions for the first 10 timesteps. The model is then allowed to freely operate all flexible plants and adjust initial reservoir conditions until timestep $u = 361$, or hour $t = 1$, the first timestep at which power exports and imports to or from the grid are measured. In cases where flexible operations are disabled, all operational decision variables are held at their initial conditions for all timesteps.

$$x_{c,u=1:10}^{PROD} = p_c^{BaseProd} \cdot \frac{y_c^{BASE}}{p_c^{Cap}} \tag{3a}$$

$$x_{c,u=1:10}^{PPRESSURE} = p_c^{MinPPressure} \cdot \frac{y_c^{BASE}}{p_c^{Cap}} \tag{3b}$$

$$x_{c,u=1:10}^{IPRESSURE} = p_c^{MinIPressure} \cdot \frac{y_c^{BASE}}{p_c^{Cap}} \tag{3c}$$

$$x_{c,u=1:10}^{PUP1} = 0 \tag{3d}$$

$$x_{c,u=1:10}^{PUP2} = 0 \tag{3e}$$

$$x_{c,u=1:10}^{PUP3} = 0 \tag{3f}$$

$$x_{c,u=1:10}^{PDN1} = 0 \tag{3g}$$

$$x_{c,u=1:10}^{PDN2} = 0 \tag{3h}$$

$$x_{c,u=1:10}^{PDN3} = 0 \tag{3i}$$

Eq. (3a) sets the starting production flow rate to be equal to the steady-state flow rate for a baseload plant of capacity y^{BASE}. Eq. (3b) and Eq. (3c) do the same for the production and injection bottomhole pressures, setting the initial bottomhole pressures equal to the model's minimum allowable pressures. Pressure variables are scaled with installed capacity and thus do not represent true bottomhole pressures. Eqs. (3d) through (3i) fix the initial injection rate to be equal to the steady-state injection rate.

Supplementary Note 3.2.3: Pressure Formulation

The constraints describing pressure evolution in response to changes in pumping are central to the accurate representation of geothermal flexibility. These represent the pressure at each well bottomhole as a superposition of linearized pressure response functions referencing changes in pumping rates during the previous 50 timesteps. The motivation, justification and validation of this approach are described in Ricks et al. [21]. For the purpose of retaining computational tractability when running GenX with the geothermal IRES module, we reduce the number of look-back timesteps in the pressure formulation to 50 from the 200 used in Ricks et al. [21]. We find that doing so improves solution times significantly while changing outcomes of interest (system cost, EGS deployment) by less than 0.1%.

$$x_{c,u}^{PPRESSURE} = x_{c,u-1}^{PPRESSURE} + (x_{c,u-1}^{PROD} - x_{c,u}^{PROD}) \cdot (p_{c,0}^{pp} - p_c^{ss}) - \sum_{a \in [1:50]} \Big((x_{c,u-a}^{PROD} - x_{c,u-a-1}^{PROD}) \cdot (p_{c,a}^{pp} - p_c^{ss}) + (e_{c,u-a-1}^{INJ} - e_{c,u-a}^{INJ}) \cdot (p_{c,a}^{ip} - p_c^{ss}) \Big) + ((x_{c,u-1}^{PROD} - p_c^{BaseProd}) - (e_{c,u-1}^{INJ} - 60)) \cdot \frac{y_c^{BASE}}{p_c^{Cap}} \cdot p_c^{ss} - e_{c,u}^{Leakoff\_Prod} \quad \forall c \in C, u \in U \tag{4a}$$

$$x_{c,u}^{IPRESSURE} = x_{c,u-1}^{IPRESSURE} - (e_{c,u-1}^{INJ} - x_{c,u}^{INJ}) \cdot (p_{c,0}^{ii} - p_c^{ss}) - \sum_{a \in [1:50]} \Big((x_{c,u-a}^{PROD} - x_{c,u-a-1}^{PROD}) \cdot (p_{c,a}^{pi} - p_c^{ss}) + (e_{c,u-a-1}^{INJ} - e_{c,u-a}^{INJ}) \cdot (p_{c,a}^{ii} - p_c^{ss}) \Big) + ((x_{c,u-1}^{PROD} - p_c^{BaseProd}) - (e_{c,u-1}^{INJ} - 60)) \cdot \frac{y_c^{BASE}}{p_c^{Cap}} \cdot p_c^{ss} - e_{c,u}^{Leakoff\_Inj} \quad \forall c \in C, u \in U \tag{4b}$$

$$e_{c,u}^{Leakoff\_Prod} = \Big(x_{c,u}^{PPRESSURE} - p_c^{MinPPressure} \cdot \frac{y_c^{BASE}}{p_c^{Cap}} \Big) \cdot p^{MaxLeakoff} \quad \forall c \in C, u \in U \tag{4c}$$

$$e_{c,u}^{Leakoff\_Inj} = \Big(x_{c,u}^{IPRESSURE} - p_c^{MinIPressure} \cdot \frac{y_c^{BASE}}{p_c^{Cap}} \Big) \cdot p^{MaxLeakoff} \quad \forall c \in C, u \in U \tag{4d}$$

$$x_{c,v}^{PPRESSURE} \leq x_{c,9120}^{PPRESSURE} \quad \forall c \in C, v \in [337:360] \tag{4e}$$

$$x_{c,v}^{IPRESSURE} \leq x_{c,9120}^{IPRESSURE} \quad \forall c \in C, v \in [337:360] \tag{4f}$$

Eq. (4a) describes the production well bottomhole pressure at timestep u as a function of the its value at the previous timestep and the cumulative effects of injection and production flow rate changes at previous timesteps, and Eq. (4b) does the same for injection well bottomhole pressure. The first line of each constraint references the pressure at the previous timestep, as well as an "instantaneous" (i.e. on a timescale much less than an hour) change in pressure due to pumping on the same well at the current timestep. The second and third lines capture the superimposed effects of all production and injection rate changes at the previous 50 timesteps. The fourth line references the difference between the net pumping rate into the reservoir at the previous timestep and the steady-state net pumping rate, which captures the lingering cumulative effects of changes in pumping at all previous timesteps. The final line incorporates an excess leakoff rate due to elevated reservoir pressure. This rate is given in Eqs. (4c) and (4d), and is assumed to increase linearly for pressures above the reservoir's baseline in steady-state operation. The parameter determining the magnitude of leakoff, $p^{MaxLeakoff}$, is set to 0 by default, as this excess leakoff formulation is only used in sentitivity cases. Eqs. (4e) and (4f) force all flexible geothermal plants to maintain reservoir pressures at the last modeled hour that are greater than or equal to the pressures at the 24 timesteps immediately preceding the first modeled hour. This constraint ensures that reservoir pressures 'loop' over the modeled weather year, preventing flexible geothermal plants from extracting additional value by ending the year with a lower reservoir pressure than they began with.

Supplementary Note 3.2.4: Production Rate and Generation

Production flow rate is limited by production well bottomhole pressure, while *usable* production flow is constrained by the surface plant capacity. Production flow is converted to electricity generation with an efficiency determined by the properties of the resource cluster and the current ambient temperature. Net generation exportable to the grid is constrained by the size of the plant's grid interconnection.

$$x_{c,u}^{PROD} \leq p_c^M \cdot x_{c,u}^{PPRESSURE} + p_c^B \qquad \forall c \in C, u \in U \qquad (5a)$$

$$e_{c,t}^{IRES\_NoVar} = \frac{p_c^{Cap}}{p_c^{BaseProd}} \cdot x_{c,t+360}^{PROD} \qquad \forall c \in C, t \in T \qquad (5b)$$

$$e_{c,t}^{IRES\_NoVar} <= (y_c^{BASE} + y_c^{FLEX}) \cdot p_c^{Peaking} \qquad \forall c \in C, t \in T \qquad (5c)$$

$$x_{c,c}^{P\_IRES} \leq e_{c,t}^{IRES\_NoVar} \cdot p_{c,t}^{IresVar} \qquad \forall c \in C, t \in T \qquad (5d)$$

$$e_{c,t}^{IRES\_Net} = x_{c,t}^{P\_IRES} - x_{c,t}^{PP\_IRES} \qquad \forall c \in C, t \in T \qquad (5e)$$

$$e_{c,t}^{IRES\_NET} \leq x_c^{IC} \qquad \forall c \in C, t \in T \qquad (5f)$$

Eq. (5a) constrains the geofluid production rate to be less than or equal to a linear function of production well bottomhole pressure. Eq. (5b) sets the generation (before considering ambient temperature effects) at the current timestep based on the surface plant standard brine effectiveness and the current production flow rate. Eq. (5c) constrains e^{IRES_NoVar} to be less than or equal to the total installed surface plant capacity multiplied by a peaking factor. For the present work we assume a peaking factor of 1.1, reflecting an organic rankine cycle plant's ability accept geofluid flow rates up to 10% above its design point without significant efficiency losses [22, 23]. Eq. (5d) constrains the surface plant net generation (not inclusive of injection pumping load), to be less than or equal to the current maximum potential generation, which is found by multiplying e^{IRES_NoVar} by the current ambient temperature-based capacity factor multiplier. Eq. (5e) expresses the net generation contributed to the local GenX power balance as the difference between plant generation and injection pumping load, and Eq. (5f) constrains this to be less than or equal to the plant's grid interconnection capacity.

Supplementary Note 3.2.5: Injection Rate and Parasitic Load

The parasitic power requirement for injection pumping is nonlinearly dependent on both the injection pumping rate and injection wellhead pressure. We approximate this nonlinear relationship through a piecewise approach utilizing six variables representing deviations from the steady-state injection rate at various levels.

$$e_{c,u}^{INJ} = 60\frac{x_c^{BASE}}{p_c^{Cap}} + x_{c,u}^{PUP1} + x_{c,u}^{PUP2} + x_{c,u}^{PUP3} - x_{c,u}^{PDN1} - x_{c,u}^{PDN2} - x_{c,u}^{PDN3} \qquad \forall c \in C, u \in U \qquad (6a)$$

$$x_{c,u}^{PDN1} \leq 20\frac{x_c^{BASE}}{p_c^{Cap}} \qquad \forall c \in C, u \in U \qquad (6b)$$

$$x_{c,u}^{PDN2} \leq 20\frac{x_c^{BASE}}{p_c^{Cap}} \qquad \forall c \in C, u \in U \qquad (6c)$$

$$x_{c,u}^{PDN3} \leq 20\frac{x_c^{BASE}}{p_c^{Cap}} \qquad \forall c \in C, u \in U \qquad (6d)$$

$$x_{c,u}^{PUP1} \leq 20\frac{x_c^{BASE}}{p_c^{Cap}} \qquad \forall c \in C, u \in U \qquad (6e)$$

$$x_{c,u}^{PUP2} \leq 20\frac{x_c^{BASE}}{p_c^{Cap}} \qquad \forall c \in C, u \in U \qquad (6f)$$

$$x_{c,u}^{PUP3} \leq 20\frac{x_c^{BASE}}{p_c^{Cap}} \qquad \forall c \in C, u \in U \tag{6g}$$

$$x_{c,u}^{PUP3} \leq x_{c,u}^{PUP2} \qquad \forall c \in C, u \in U \tag{6h}$$

$$x_{c,u}^{PUP2} \leq x_{c,u}^{PUP1} \qquad \forall c \in C, u \in U \tag{6i}$$

$$x_{c,u}^{PDN3} \leq x_{c,u}^{PDN2} \qquad \forall c \in C, u \in U \tag{6j}$$

$$x_{c,u}^{PDN2} \leq x_{c,u}^{PDN1} \qquad \forall c \in C, u \in U \tag{6k}$$

$$\begin{aligned} e_{c,t}^{IRES\_PumpPower} = {} & (x_{c,t+360}^{IPRESSURE} - p_c^{Hydrostatic} \cdot \frac{x_c^{BASE}}{p_c^{Cap}}) \cdot p^{IPF} \cdot 60 - \\ & (p_c^{WellPres1} - p_c^{WellPres0}) \cdot p^{IPF} \cdot x_{c,t+360}^{PDN1} - \\ & (2p_c^{WellPres2} - p_c^{WellPres1}) \cdot p^{IPF} \cdot x_{c,t+360}^{PDN2} - \\ & (3p_c^{WellPres3} - 2p_c^{WellPres2}) \cdot p^{IPF} \cdot x_{c,t+360}^{PDN3} + \\ & (p_c^{MaxIPressure} - p_c^{Hydrostatic} + 4p_c^{WellPres4} - 3p_c^{WellPres3}) \cdot p^{IPF} \cdot x_{c,u}^{PUP1} + \\ & (p_c^{MaxIPressure} - p_c^{Hydrostatic} + 5p_c^{WellPres5} - 4p_c^{WellPres4}) \cdot p^{IPF} \cdot x_{c,u}^{PUP2} + \\ & (p_c^{MaxIPressure} - p_c^{Hydrostatic} + 6p_c^{WellPres6} - 5p_c^{WellPres5}) \cdot p^{IPF} \cdot x_{c,u}^{PUP3} \end{aligned} \qquad \forall c \in C, u \in U \tag{6l}$$

$$x_{c,t}^{PP\_IRES} \geq e_{c,t}^{IRES\_PumpPower} \qquad \forall c \in C, t \in T \tag{6m}$$

$$x_{c,t}^{PP\_IRES} \leq y_c^{PUMP} \qquad \forall c \in C, t \in T \tag{6n}$$

$$x_{c,u}^{INJSQ} \geq 120e_{c,u}^{INJ} - 3600\frac{x_c^{BASE}}{p_c^{Cap}} \qquad \forall c \in C, t \in T \tag{6o}$$

$$x_{c,u}^{INJSQ} \geq 80e_{c,u}^{INJ} - 1600\frac{x_c^{BASE}}{p_c^{Cap}} \qquad \forall c \in C, t \in T \tag{6p}$$

$$x_{c,u}^{INJSQ} \geq 40e_{c,u}^{INJ} - 400\frac{x_c^{BASE}}{p_c^{Cap}} \qquad \forall c \in C, t \in T \tag{6q}$$

$$x_{c,u}^{INJSQ} \geq 160e_{c,u}^{INJ} - 6400\frac{x_c^{BASE}}{p_c^{Cap}} \qquad \forall c \in C, t \in T \tag{6r}$$

$$x_{c,u}^{INJSQ} \geq 200e_{c,u}^{INJ} - 10000\frac{x_c^{BASE}}{p_c^{Cap}} \qquad \forall c \in C, t \in T \tag{6s}$$

$$x_{c,u}^{INJSQ} \geq 240e_{c,u}^{INJ} - 14400\frac{x_c^{BASE}}{p_c^{Cap}} \qquad \forall c \in C, t \in T \tag{6t}$$

$$\sum_{u \in [361:U]} x_{c,u}^{INJSQ} \leq 3600\frac{x_c^{BASE}}{p_c^{Cap}} \cdot T \tag{6u}$$

Eq. (6a) formulates injection rate at hour t in terms of deviations from the steady-state injection rate, which is 60 STB/min per injection well. Eqs. (6b) through (6g) cap the variables controlling deviations from the steady-state injection rate at 1/3 of the steady-state rate. Eqs. (6h) through (6k) help ensure

that the deviations are activated in the correct order, i.e. the second segment of injection reduction can only be activated after the first has been activated. Eq. (6l) approximates the theoretical injection pumping power requirement. The first line expresses power required to pump at the steady-state injection rate on the current injection well bottomhole pressure as the product of these quantities and the pump power conversion factor. The next three lines deal with reductions in this load due to reductions in injection rate, which are calculated based on the minimum injection well bottomhole pressure and the current injection rate. The final three lines deal with increases in injection load due to increased injection rate, which are calculated based on the maximum injection well bottomhole pressure and the current injection rate. As detailed in Ricks et al. [21], Eq. (6l) is always a slight over-approximation of the true nonlinear equation for injection pumping power. Eq. (6m) requires the parasitic load from injection pumping to be greater than the theoretical injection pumping power requirement. These expressions are not set equal because injection pumping load must always be greater than or equal to 0, while the theoretical power requirement could be less than zero due to thermosiphon effects. Eq. (6n) requires that the injection pumping load always be less than or equal to the installed injection pump power capacity. Eqs. (6o) through (6t) bound the variable $x_{c,u}^{INJSQ}$ from below, via a six-part piecewise linearization of the square of $e_{c,u}^{INJ}$. Eq. (6u) then requires that the sum of this squared injection rate over the modeled year be less than or equal to its sum under a steady-state injection rate. This requirement ensures that the flexible geothermal plant experiences a long-term thermal drawdown rate no greater than that of an inflexible plant [24].

Supplementary Note 3.2.6: Surface Geofluid Storage

The potential for mismatch between geofluid injection and production rates means that there must be a means of storing excess produced geofluid. We assume that this is accomplished via steel tanks sited at the surface facility. When more geofluid is injected than is produced, the storage level will decrease. Because of subsurface fluid leakoff, the plant will consume water on net over the year. We assume that additional makeup water is consumed whenever the plant's injection rate exceeds its production rate and the geofluid storage level is 0.

$$x_{c,1}^{GFS} = 0 \qquad \forall c \in C \tag{7a}$$

$$x_{c,t}^{GFS} = x_{c,t-1}^{GF} + (x_{c,t+360}^{PROD} - e_{c,t+360}^{Inj}) \cdot \gamma + x_{c,t}^{GFM} \qquad \forall c \in C, t \in [2:8760] \tag{7b}$$

$$x_{c,t}^{GFS} \leq\leq y_c^{TANK} \qquad \forall c \in C, t \in T \tag{7c}$$

$$\tag{7d}$$

Eq. (7a) sets the starting level of surface geofluid storage at 0. Eq. (7b) expresses the storage level at all subsequent timesteps as the sum of the previous timestep's storage level and the current timestep's net additions and withdrawals. Here, γ converts between flow rates in STB/min and total geofluid consumption in millions of liters. Geofluid can be removed from storage when wellfield injection is greater than production, and can be added to storage when production is greater than injection, or when makeup water is imported. Eq. (7c) ensures that the amount of stored fluid never exceeds the total installed storage capacity.

Supplementary Note 3.2.7: System Capacity Reserve Margin Contribution

For GenX runs that include a capacity reserve margin policy, EGS generators are credited for contributing to the required level of regional capacity availability at every model timestep. As with other dispatchable generators, flexible EGS is credited based on the maximum amount of power it could have provided in a given hour, multiplied by a derating factor of 0.9. The capacity contribution from all EGS generators in a given region is added to the GenX capacity reserve margin constraint for that region.

$$x_{c,u}^{MAXPROD} \leq p_c^M \cdot x_{c,u}^{PPRESSURE} + p_c^B \qquad \forall c \in C, u \in U \qquad (8a)$$

$$e_{c,t}^{IRES\_MaxNoVar} = \frac{p_c^{Cap}}{p_c^{BaseProd}} \cdot x_{c,t+360}^{MAXPROD} \qquad \forall c \in C, t \in T \qquad (8b)$$

$$e_{c,t}^{IRES\_MaxNoVar} <= (y_c^{BASE} + y_c^{FLEX}) \cdot p_c^{Peaking} \qquad \forall c \in C, t \in T \qquad (8c)$$

$$x_{c,t}^{MAXP\_IRES} \leq e_{c,t}^{IRES\_MaxNoVar} \cdot p_{c,t}^{IresVar} \qquad \forall c \in C, t \in T \qquad (8d)$$

$$e_{r,t}^{IRES\_CapRes} = \sum_{c \in C} p_{c,r}^{CapRes} (x_{c,t}^{MAXP\_IRES} - x_{c,t}^{PP\_IRES}) \qquad \forall r \in R, t \in T \qquad (8e)$$

$$(8f)$$

Eq. (8a) constrains the maximum geofluid production rate to be less than or equal to a linear function of production well bottomhole pressure. Eq. (8b) sets the maximum generation (before considering ambient temperature effects) at the current timestep based on the surface plant standard brine effectiveness and the current maximum production flow rate. Eq. (8c) constrains $e^{IRES\_MaxNoVar}$ to be less than or equal to the total installed surface plant capacity multiplied by a peaking factor. Eq. (8d) constrains the maximum surface plant net generation (not inclusive of injection pumping load), to be less than or equal to the current maximum potential generation, which is found by multiplying $e^{IRES\_MaxNoVar}$ by the current ambient temperature-based capacity factor multiplier. Eq. (8e) expresses the aggregate capacity contribution of all EGS plants in the system to each capacity reserve margin constraint, which is calculated by multiplying the constraint's multiplier (either 0.9 or 0) with the net of maximum possible gross power output and actual pumping power consumption in the current timestep.

Supplementary Note 4: Flexible Geothermal Reservoir Simulation

We use ResFrac, a commercial reservoir simulator, to quantify the behavior of an EGS reservoir undergoing flexible operations. Detailed discussions of the simulator are provided in McClure and Kang [25] and McClure et al. [26]. Here, we provide a brief overview of the governing equations and numerical methods.

ResFrac is a fully-compositional, thermal, and geomechanical reservoir model. It integrates fluid flow in the wellbores, fluid flow in the reservoir, heat transfer in the reservoir, and mechanical deformation of the pore volume and fractures in the subsurface. The governing equations involve momentum balance for flow in the wellbore, mass balance for flow in the reservoir, energy balance for heat transfer in the reservoir, and momentum balance for mechanical deformation of the reservoir.

The system is discretized numerically using one-dimensional elements along the wellbore, three-dimensional volumetric elements for the reservoir matrix, and two-dimensional surface area elements for the fractures. Fluid flow and heat transfer are calculated using a finite volume method. Fracture deformation is calculated using a boundary element method. In this study, as in Ricks et al. [21], we use a Cartesian mesh for the reservoir matrix volume and a fracture mesh of rectangular elements. Solving this system of equations allows us to calculate fluid pressure along the wellbore (along with flowing friction), the fluid pressure distribution in the reservoir and fracture volume, the temperature distribution in the reservoir and fracture volume, and the mechanical deformation of the fractures.

In the present work, we simulate a single representative geothermal reservoir system consisting of horizontal injection and production wells arrayed in a "wine rack" formation (Supplementary Figure 27). The horizontal well pattern consists of alternating injection and production wells in order to optimize the heat sweep between wells. Each wellbore has a lateral section that is 2286 m in length, and the laterals are offset by 305 m horizontally and 152 m vertically. The production wells are placed slightly shallower than the injection wells. The wells are connected by a uniform network of vertical fractures, with 150 fractures placed at 15 m intervals along each injection well horizontal section. We simulate an indefinitely-long wine rack by setting up a system of two injection wells and three production wells, with no-flow boundary conditions imposed on vertical planes intersecting the outer two production wells. These no-flow boundaries are located exactly at the midpoint of the well spacing, and therefore the model symmetry replicates the hydraulic properties of an indefinitely long reservoir.

We assume that the reservoir is fully-saturated with single phase water in a low porosity (0.05) formation. In the mid-case subsurface favorability scenario vertical matrix permeability is set to 2.0×10^{-18}

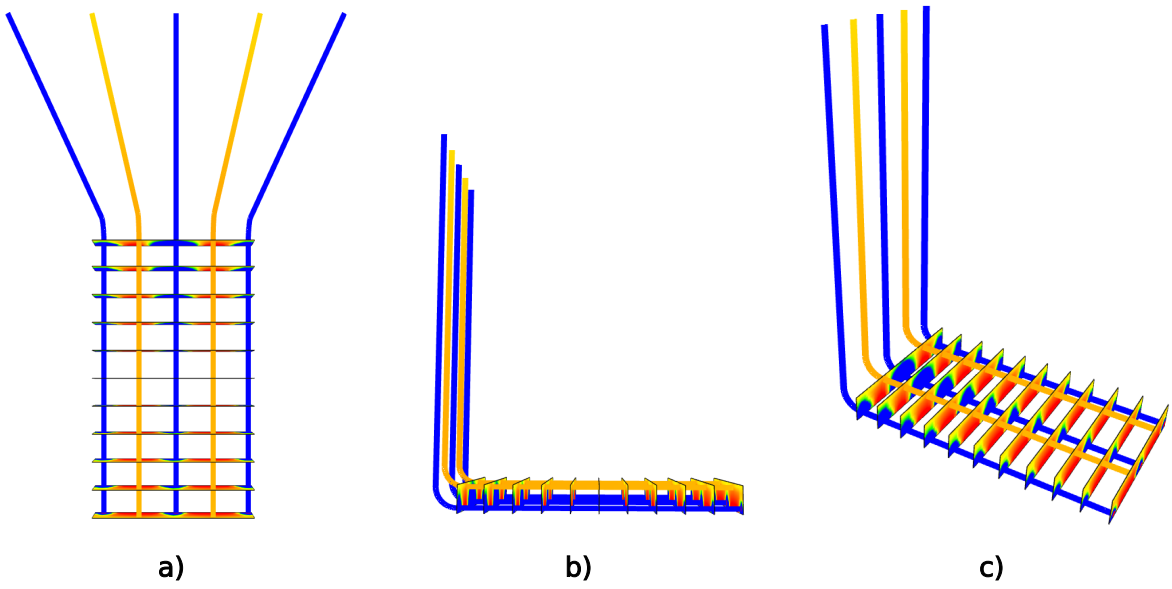

Supplementary Figure 27: Vertical (a), horizontal (b), and diagonal (c) views of the at-scale EGS reservoir design simulated in this work. Production and injection wells are shown in orange and blue, respectively, and well laterals are connected by an engineered fracture network. For visual clarity, only every 15th fracture is shown.

m^2 and horizontal permeability to 1.0×10^{-17} m^2. These conditions are intended to be representative of a typical low-permeability reservoir from which heat cannot be extracted without prior stimulation. We assume in the mid-case subsurface favorability scenario that the fractures created by the stimulation treatment have a conductivity of 4.5×10^{-13} m^3. In the high and low subsurface favorability scenarios we increase/decrease permeability by two orders of magnitude and double/halve the assumed fracture conductivity, respectively.

We run baseline simulations in a model reservoir with a central depth of 3 km and a central temperature of 204.4 C (400 F) and use these to measure the transient pressure response functions at the injection and production well bottomholes due to changes in injection and production flow rates. After the reservoir system is allowed to come into equilibrium over a period of multiple years, we restrict flow rates from the production wells to 52% of the steady-state average while maintaining injection rates for a period of 240 hours. During this period we measure the pressure increases at the injection and production well bottomholes at hourly intervals, interpolating where necessary. These are divided by the step change in production flow rate to find the normalized pressure response coefficients described in Section 3.2.3. We repeat this process to quantify the pressure response to changes in injection flow rates, increasing injection flow in both wells by 33% for a 240 hour period while fixing production flow rates at their steady-state value. Two simulations are run with identical operations to measure pressure response functions in the high and low subsurface favorability cases. As in Ricks et al. [21], the linearized pressure response functions are validated through reproduction of numerical reservoir simulation results. One such reproduction is shown in Supplementary Figure 28. All simulation-derived data used as inputs for GenX in this study, including hourly pressure response coefficients for each subsurface favorability case, are available at Ricks et al. [3]. High and low subsurface favorability cases are also used to measure the change in pressure across the reservoir due to higher or lower fracture conductivity. This effect is relatively small: a decrease of 0.49 MPa in the high subsurface favorability case and an increase of 1.08 MPa in the low subsurface favorability case. It is assumed for the purpose of this work that the change in pressure loss and the bottomhole pressure response functions remain roughly constant regardless of depth and resource temperature.

We additionally run six sensitivity cases for reservoir depths from 1.5 km to 6.5 km at 1 km intervals. We use these to find the maximum achievable production flow rate as a function of production well

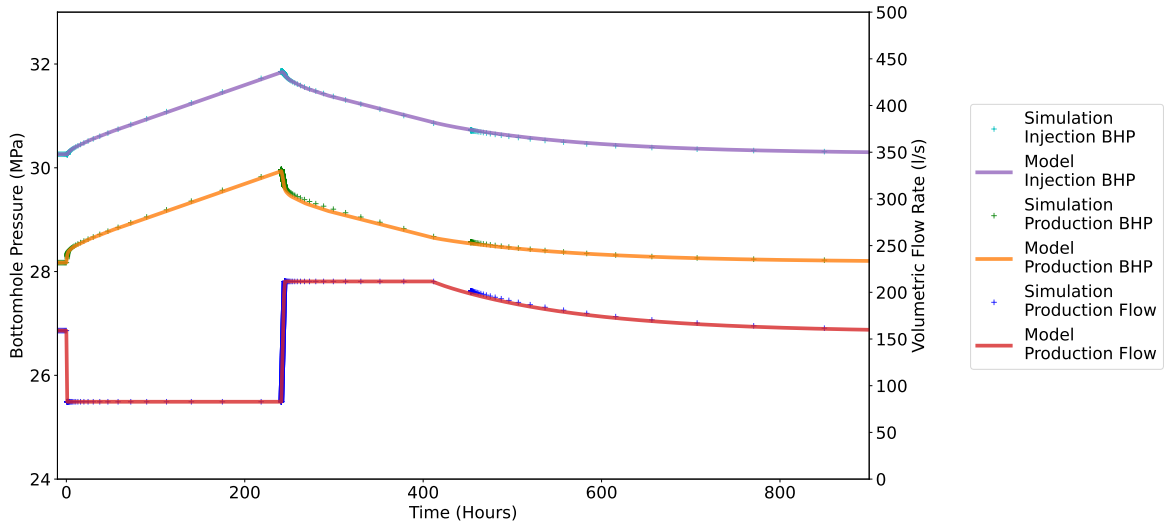

Supplementary Figure 28: Replication of numerical reservoir simulation results in the linear optimization model, for the mid- subsurface favorability case. Simulation results are shown as point data and model results as continuous data.

bottomhole pressure at each depth, which is accomplished by allowing unrestricted flow after the bottomhole pressure has built up over a 240-hour period and observing the simultaneous decline of pressure and flow rate. The relationship is nonlinear but smooth, and we fit to a linear function for the purpose of computational tractability in this work (see Section 3.2.4). We also use the depth sensitivity cases to find the change in injection wellhead pressure as a function of injection flow rate at each depth, as described in Section 3.2.5. We step injection flow rates down from the steady state rate to 50% at four equal intervals and fit the measured relationship between injection flow rate and the pressure drop across the injection well to Bernoulli's equation for turbulent pipe flow with friction. This approach captures the nonlinear increase in injection wellhead pressure and injection pumping power with increasing injection flow rate.

Finally, we run sensitivity cases varying reservoir temperature to quantify the impact of the thermosiphon effect on injection wellhead pressure (and by extension on injection pumping power). The low and high temperature sensitivity cases simulate starting reservoir temperatures of 185 C (365 F) and 224 C (435 F), respectively. We find the change in required injection wellhead pressure as a function of reservoir temperature based on a linear fit of these cases and the baseline case. We also account for the change in production wellhead pressure needed to prevent produced geofluid from flashing to steam at a given temperature, and by extension the change in injection wellhead pressure needed to maintain flow rate. The flash point pressure adjustment is extracted from steam tables and added to the thermosiphon adjustment to produce a final adjustment to the baseline injection wellhead pressure as a function of resource temperature.

Supplementary Note 5: EGS Costing

Supplementary Note 5.1: Wellfield Cost

Geothermal well costs are derived as a function of reservoir depth from well cost functions originally presented in Lowry et al. [27] and developed to support the Department of Energy's GeoVision report [28]. We derive costs for both injection and production wells with target depths from 1.5 km to 6.5 km at 1 km intervals. All wells are assumed to terminate in 2286 m horizontal sections at the target depth. We update well cost curves from Lowry et al. [27] to reflect drilling cost declines in the last several years by multiplying by the ratio of the 2019 oil and gas well drilling services production price index (BLS Series WPU60110301) to the PPI assumed in Lowry et al. [27]. We interpolate between the original curves for small diameter (21.59 cm production zone hole) and large diameter (31.12 cm production zone hole) wells to derive costs for 24.45 cm diameter wells, which is the production zone hole diameter assumed in the reservoir simulations used in this work.

Wells in Lowry et al. [27] are assumed to end in a 305 m cased horizontal production interval. For each

target depth we add the cost from the additional 1981 m of horizontal extent assumed in our reservoir model. This is calculated based on the slope of the well cost function at the target depth, the added cost per hour for horizontal drilling assumed in Lowry et al. [27], and an assumed drilling time equal to the quoted drilling time of a vertical section of the same length. Horizontal sections for production wells are assumed to be uncased and are only 60% the cost of injection well horizontals.

Our Baseline scenario drilling costs are based on the Baseline well cost curve from Lowry et al. [27], which is intended to represent the current state-of-the-art. This curve assumes a rate of penetration (ROP) of 7.62 m/hr, which has already been surpassed in deep wells drilled in granite at the Utah FORGE EGS test site using polycrystalline diamond drill bits [29]. Based on the FORGE results, we update the Baseline drilling curve to reflect an ROP of 15.42 m/hr. This is done using quoted reductions in cost for Baseline wells at multiple depths due to doubled ROP from Lowry et al. [27]. Our Advanced scenario drilling costs are based directly on the Intermediate II scenario from Lowry et al. [27], which assumes modestly increased ROP and major advances in well casing programs. Cost curves for both drilling scenarios are shown in Supplementary Figure 29.

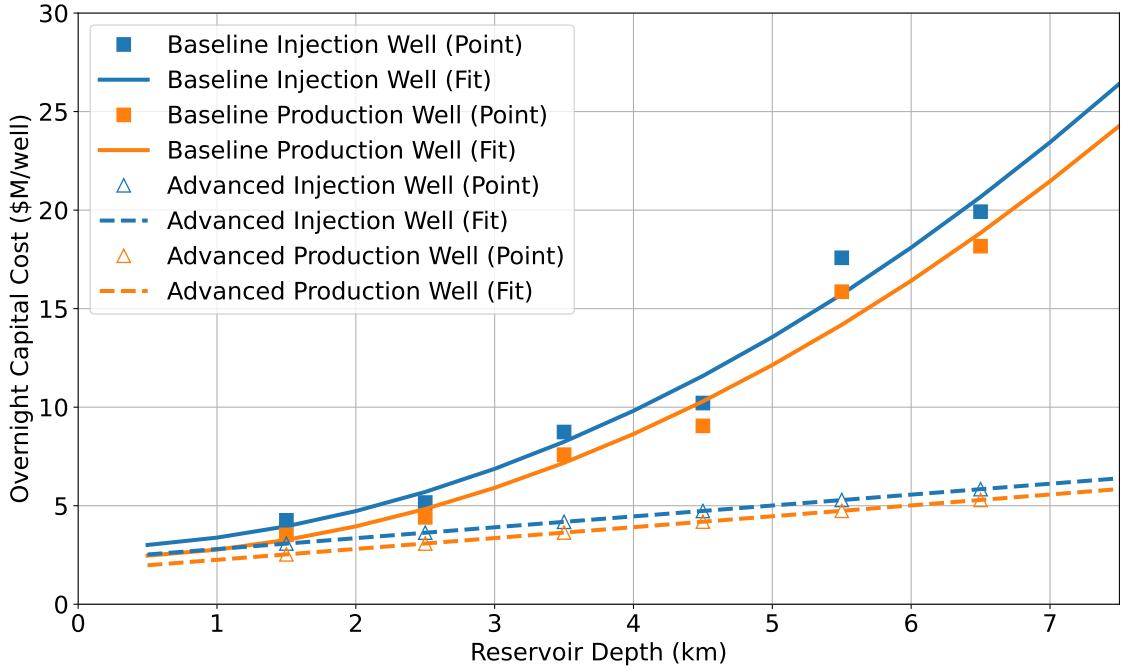

Supplementary Figure 29: Drilling cost point data and fitted curves for baseline and advanced drilling cases.

In addition to drilling costs, we assume stimulation costs of $4.5 million per injection well. This is significantly higher than the cost assumed in Lowry et al. [27], accounting for the much larger stimulated area in our assumed reservoir design. We assume that only injection wells are stimulated, and that open-hole production wells are drilled such that they intersect the fractures created during injection well stimulation. Both drilling and stimulation are assumed to have success rates of 90%. We assume a ratio of 1.2 production wells per injection well, reflecting a standardized 'wine rack' reservoir design consisting of four injection wells and five production wells.

Supplementary Note 5.2: Surface Plant Cost

We calculate surface plant cost and conversion efficiency as functions of geofluid inlet temperature using the GETEM geothermal costing model developed by NREL [30]. We derive separate cost curves for each well cost scenario and drilling depth, as the tradeoff between surface plant specific cost and 'brine effectiveness' (the electrical energy extracted per unit mass of geofluid) can be optimized based on well cost. When wells are more expensive, achieving higher brine effectiveness minimizes the cost of electricity by reducing the number of wells that must be drilled. When wells are less expensive, it is more cost effective to use cheaper surface plants that achieve lower brine effectiveness.

We assume that all surface plants are ORC units. While these have typically been used in low- to

medium-temperature geothermal applications, there are a number of examples of existing ORC plants exploiting high-temperature resources [31]. As GETEM does not provide ORC cost and performance data for resource temperatures above 200 C, we use extrapolated trends for this region based on fits of GETEM results for temperatures below 200 C. Plant specific cost and brine effectiveness curves are shown in Supplementary Figures 30 and 31, respectively, and follow similar trajectories in the high-temperature region to those reported elsewhere in the literature [32, 33]. These costs include an assumed $150/MW fixed cost for the field gathering system, 15% contingency, and are updated to reflect changes in the PPI for turbine and generator sets (BLS Series WPU1197). They do not include costs for production pumps, which are not assumed to be used, and injection pumps, for which costs are considered separately from the rest of the plant.

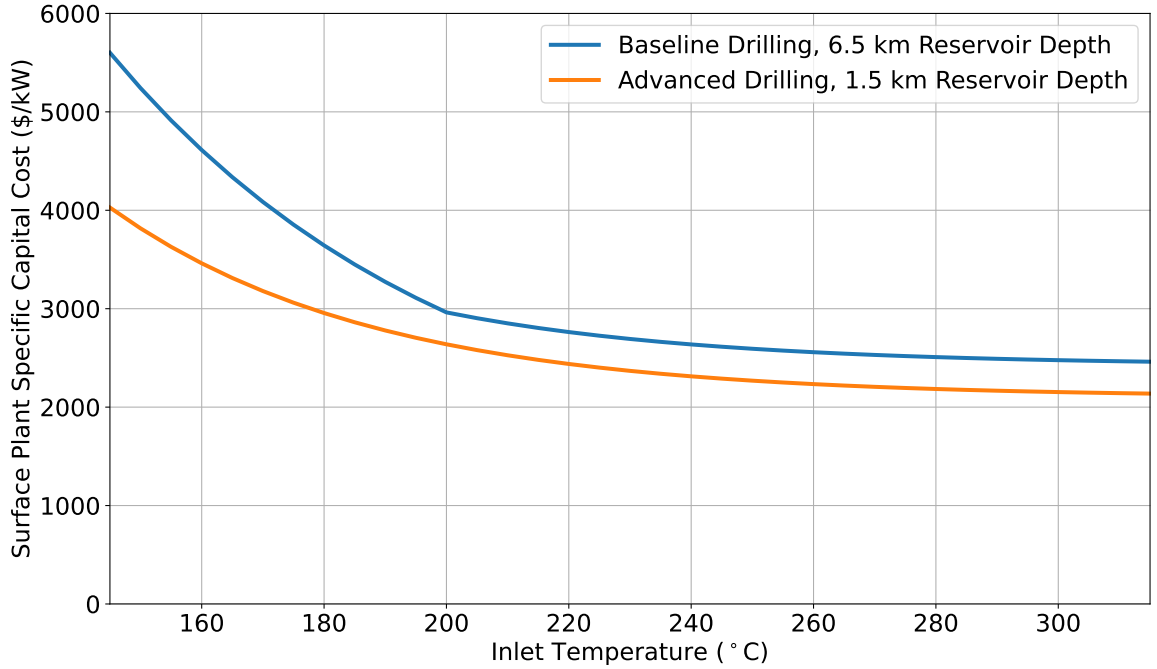

Supplementary Figure 30: Surface plant specific cost for two extreme cases - 6.5 km wells at baseline cost and 1.5 km wells at advanced cost - as a function of inlet temperature.

We assume a standard size for EGS plants of 50 MW, larger than most recent geothermal projects in the United States. Larger projects are an advantage of EGS over conventional geothermal, for which project size is constrained by the size of the local hydrothermal reservoir. GETEM assumes that specific cost for an ORC turbine-generator declines with project size up to 10 MW but is flat thereafter. Given the strong effect of production quantity on per-unit ORC costs [34], and the existence of currently-operating ORC plants as large as 100 MW [35], we assume that economies of scale continue to apply beyond the 10 MW threshold set in GETEM. We derive a functional relationship between plant size and specific cost using GETEM results for plants below the 10 MW threshold . This relationship is shown in Supplementary Figure 32, and is applied to cost and performance curves derived from GETEM results for 10 MW plants to calculate costs for larger or smaller plants.

Supplementary Note 5.3: Total Project Cost

We develop an excel costing model for this work (see 'EGS_Costing.xlsx' in Ricks et al. [3]) that calculates the annuitized investment cost and net power capacity (given in terms of megawatts per injection well) for an EGS project as a function of resource depth, resource temperature, local average ambient temperature, and drilling scenario. Given these inputs, the model calculates an adjusted geofluid inlet temperature T_{Adj} for the surface plant using the following equation:

$$T_{Adj} = T_{Res} - \Delta T_{wb} - (T_{Amb} - 10)\frac{dP/dT_{Amb}}{dP/dT_{Res}}, \tag{9}$$

where T_{Res} is the central reservoir temperature for the given resource temperature bin, ΔT_{wb} is

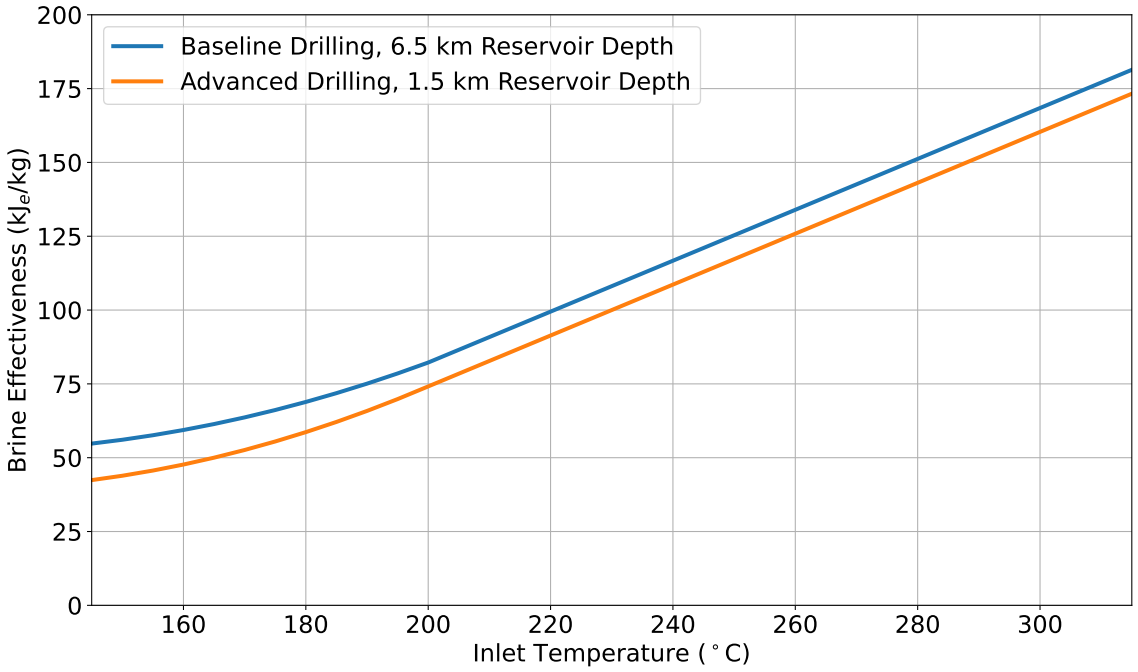

Supplementary Figure 31: Surface plant brine effectiveness for two extreme cases - 6.5 km wells at baseline cost and 1.5 km wells at advanced cost - as a function of inlet temperature.

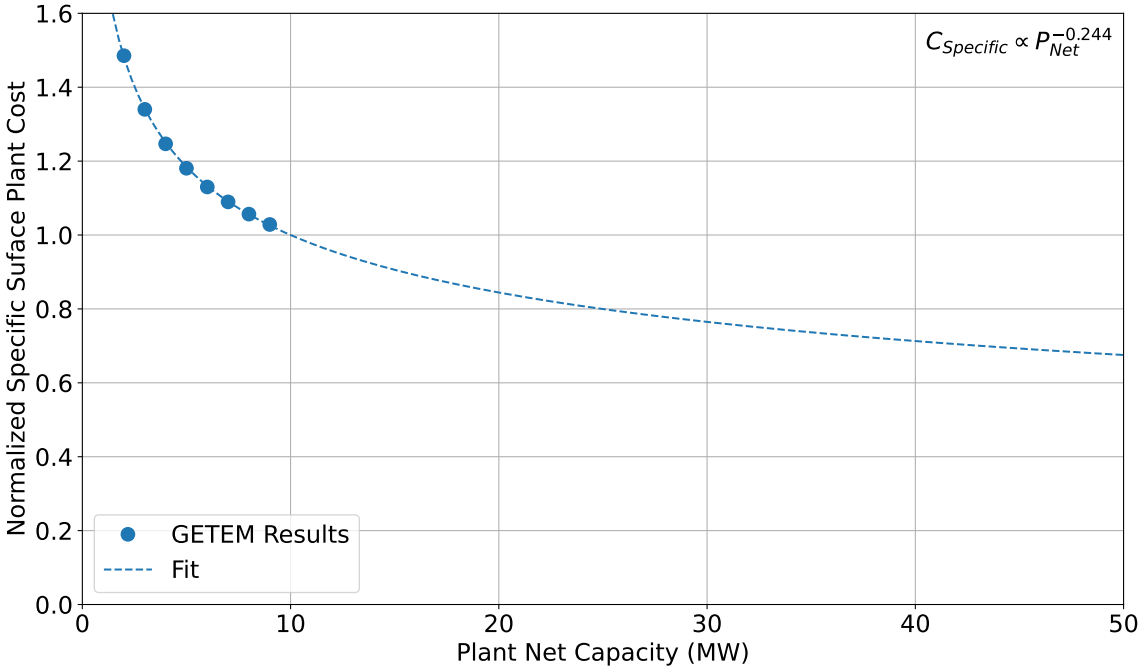

Supplementary Figure 32: Scaling relationship between surface plant specific cost and net capacity.

Development Phase	Length (Months)	Interest Rate (%)
Pre-Survey and Exploration	36	15
Test Drilling	6	15
Drilling & Stimulation	12	10
Plant Construction	12	8

Supplementary Table 9: Assumed development timeline and interest rates by phase for EGS projects.

Cost Type	Assumed Value
Wellfield O&M	1.5%/yr of wellfield overnight capital cost
Surface O&M	1.8%/yr of surface plant overnight capital cost
Taxes & Insurance	0.75%/yr of total overnight capital cost
Labor	$35000/MW-yr
Makeup Water	$300/acre-ft, multiplied by annual consumption

Supplementary Table 10: Non-investment fixed cost assumptions for EGS plants.

difference between reservoir temperature and production wellhead temperature for the given resource depth, and the final term accounts for the variation between the local average ambient temperature (see Sections 6 and 7) and the fixed 10 °C average ambient temperature assumed in GETEM. An adjustment factor is applied that converts the difference in ambient temperature to an equivalent difference in resource temperature, which can be adjusted by the user in GETEM. This factor is calculated for a given geofluid production temperature using relationships between ambient temperature, production temperature, and plant specific power from the GEOPHIRES techno-economic simulator [36]. The adjusted inlet temperature T_{Adj} and chosen reservoir depth are used to calculate surface plant specific cost and brine effectiveness based on the functional relationships described in Section 5.2. Overnight capital costs for the surface plant and wellfield are given on per-MW basis, and assume no technological learning beyond the specific advancements in drilling and reservoir engineering described above.

Construction financing costs are added to overnight capital costs based on an assumed 5.5 year development timeline, shown in Table 9. In addition to wellfield and surface plant costs we assume a pre-survey and exploration drilling cost of $250000 per project and test drilling costs of $3.3 million per project, identical to the values assumed in the GeoVision report [28]. Final CAPEX inclusive of construction financing cost is converted to an annuity assuming a 30-year financial lifetime and a real weighted average cost of capital (WACC) of 3.34%, equal to the value used for other dispatchable thermal generators (natural gas, nuclear, biomass) in the NREL ATB [15]. In addition to the annuitized capital cost, we calculate other annual fixed costs based on assumptions from GETEM [30]. These are shown in Table 10. All fixed costs are summed into a per-MW annuity representing the annual revenue required to fully pay off a project's costs over its operational lifetime. This annuity is given in terms of plant capacity at the beginning of operations.

We assume that surface plants can be oversized to provide additional flexible generating capacity when flexible operations are enabled, and that the combined capital and O&M cost of flexible surface capacity is 80% the cost of the base plant. We further assume that labor costs do not increase with the addition of flexible capacity. These choices assume that not all plant components must be oversized to enable greater geofluid throughput and power output, and that plant labor requirements do not change substantially when components are oversized. Injection pumps are not considered in total plant costs, as the sizing of these components is optimized separately based on injection pumping power requirements. We assume a fixed capital cost for injection pumps of $263/kW based on cost curves from GETEM, assuming an average pump size of 5 MW, 15% contingency, and PPI escalation following BLS Series PCU3339113339111Z4. Surface geofluid storage, which is necessary to accommodate modulations in injection and production flow rates, is also optimized separately. We adopt a cost of $0.0675/l for welded steel tanks from Belock and Mendes [37] and assume PPI escalation following BLS Series WPU101707. Capital costs for peaking capacity, injection pumps, and geofluid storage are converted to annuities using the same financing, O&M, tax and insurance assumptions as for the base surface plant. Annuities for power plant grid interconnection are calculated based on a plant's geographic location using a process described in Section 7.

Supplementary Note 6: EGS Capacity Factors

The actual generation from an EGS power plant over its lifetime will deviate significantly from its design point due to changes in geofluid temperature and local ambient weather conditions. Although air-cooled ORC power plants have many advantages, their power output fluctuates significantly based on local ambient temperature, wind speed and humidity. We model the weather dependence of EGS power plant conversion efficiency based on operational data gathered from the Dora 1 ORC geothermal power plant in Turkey [23]. We find the relationship between the deviation of local ambient air temperature from the plant's design point and the plant's net generation based on data from the plant's second year of operations. This relationship, shown in Supplementary Figure 33, indicates a strong dependence of power plant output on local air temperature. Increases in output due to lower ambient temperatures are generally smaller than the decreases in output due to elevated temperatures. We apply this relationship to all EGS power plants modeled in this study. We use historical weather data from the National Oceanic and Atmospheric Administration (NOAA) [38] to calculate an average hourly ambient temperature in a set of weather regions. These regions are based on balancing areas from the ReEDS CEM [20], which are the basic geographic layer used to develop EGS supply curves in this study (see Section 7). For each balancing area we collect hourly ambient temperature data from up to three NOAA weather stations for the 2012 weather year, the same year used to create demand and VRE generation time series in GenX. If fewer than three stations are available in a weather region we use the maximum number available. We fill in missing data points with values from 24 hours earlier before combining the hourly data from all stations in a weather region to create an average hourly temperature time series. We calculate the annual average ambient temperature in each zone and assume that this will be the design point temperature for all local EGS plants. We then create hourly capacity factor multiplier time series for local EGS power plants based on the difference between the hourly ambient temperature and the design point temperature, using the relationship shown in Supplementary Figure 33. In addition to a dependence on ambient temperatures, an EGS plant will also experience significant loss of capacity over a 30-year lifetime as thermal drawdown due to heat extraction reduces reservoir temperature. The simulated decline in output for the standard reservoir design used in this work is shown in Supplementary Figure 34. We also run additonal simulations assessing the impact of flexible production flow rate cycling on long-run thermal drawdown (see Supplementary Figure 35). The outputs indicate that cycling production while maintaining steady-state injection does not significantly alter the long-run thermal drawdown profile. We therefore assume that thermal drawdown occurs at the same rate under flexible and inflexible operations as long as injection rate is held steady. The impact of injection flexibility on long-term thermal decline is accounted for via constraints discussed in Section 3.2.5. We calculate the relationship between production temperature and power output over time for based on a linear fit of GETEM outputs for a plant with an initial reservoir temperature of 200 °C. We use the assumed WACC for EGS power plants to calculate a lifetime average capacity factor in terms of the net present value of plant generation. For the temperature decline profile shown in 34, this is 93.3%. We multiply the capacity factor multiplier time series described above by this factor to reflect the thermal drawdown over the life of a project. An example of the final capacity factor multiplier time series is shown in Supplementary Figure 36. This figure illustrates the hourly capacity factor for an inflexible geothermal power plant in the southern California weather region (ReEDS balancing area 10). There is significant diurnal variability in plant power output, as well as seasonal variability. In the winter months plant power output exceeds nameplate capacity, even with thermal drawdown taken into account. In the summer, actual power output can be as low as 60% of nameplate capacity. We note that these calculations assume a constant production fluid temperature over the modeled year, rather than one that varies slightly with production flow rate as shown in Supplementary Figure 35. While it is possible to calculate production temperature as a function of flow rate, this introduces nonlinearities that cannot be represented in a linear optimization model. This abstraction leads to the model slightly underestimating production temperature (and therefore power output) during periods of high flow, and overestimating it during periods of low flow. Because flexible plants choose to produce at higher rates during periods when the value of generation is greater, this over/underestimation of output will cause the modeled value of flexibility to be somewhat lower than in reality.

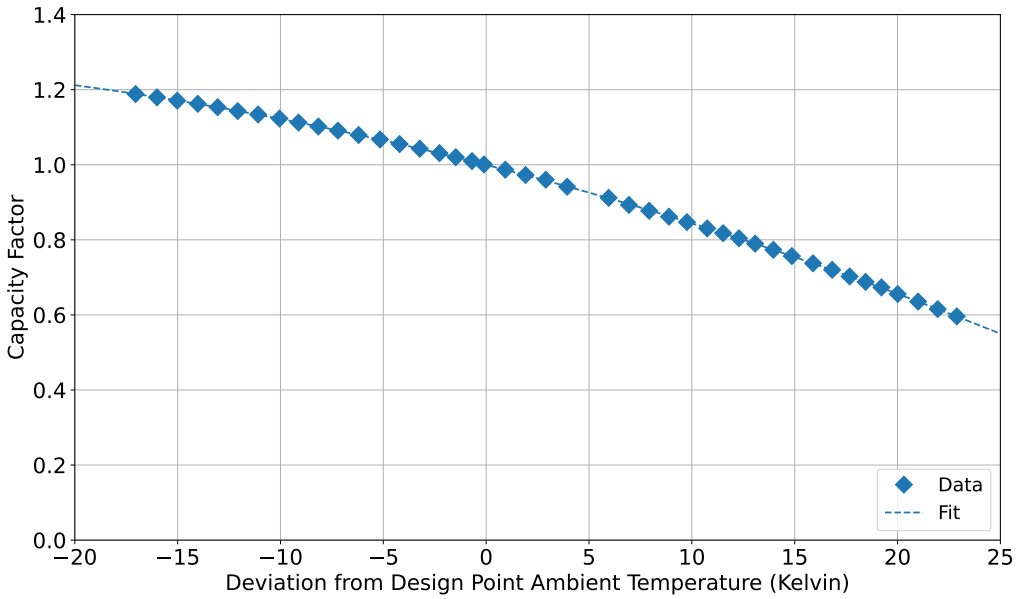

Supplementary Figure 33: Relationship between local ambient air temperature and ORC power plant generation.

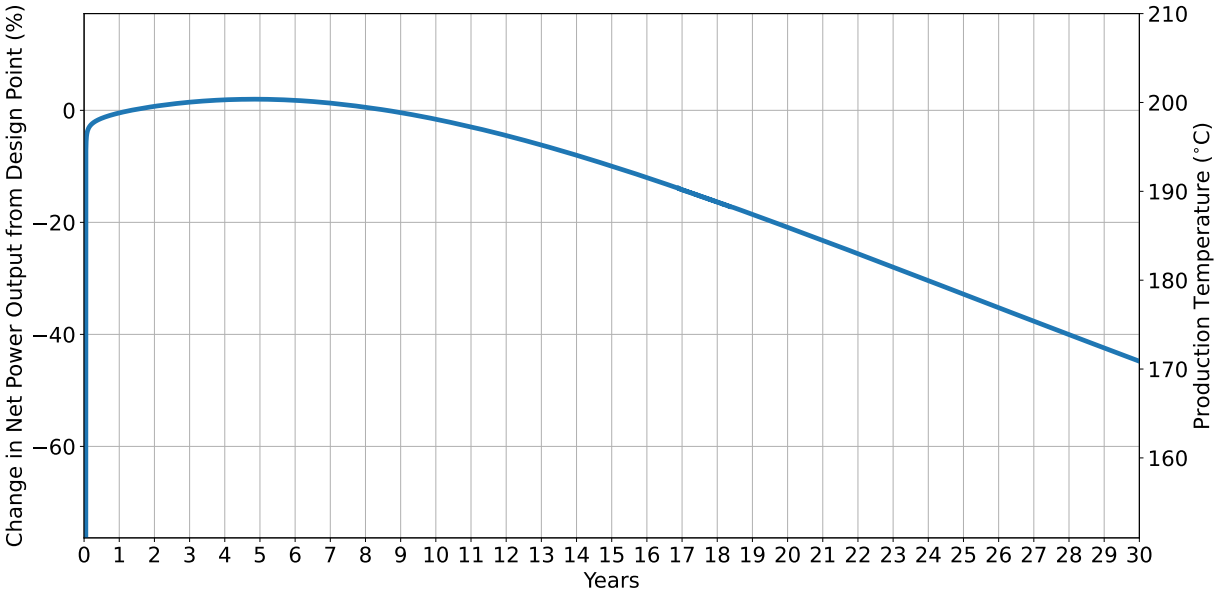

Supplementary Figure 34: Evolution of plant net power output and production wellhead temperature over 30 years of steady-state operation under baseline reservoir conditions.

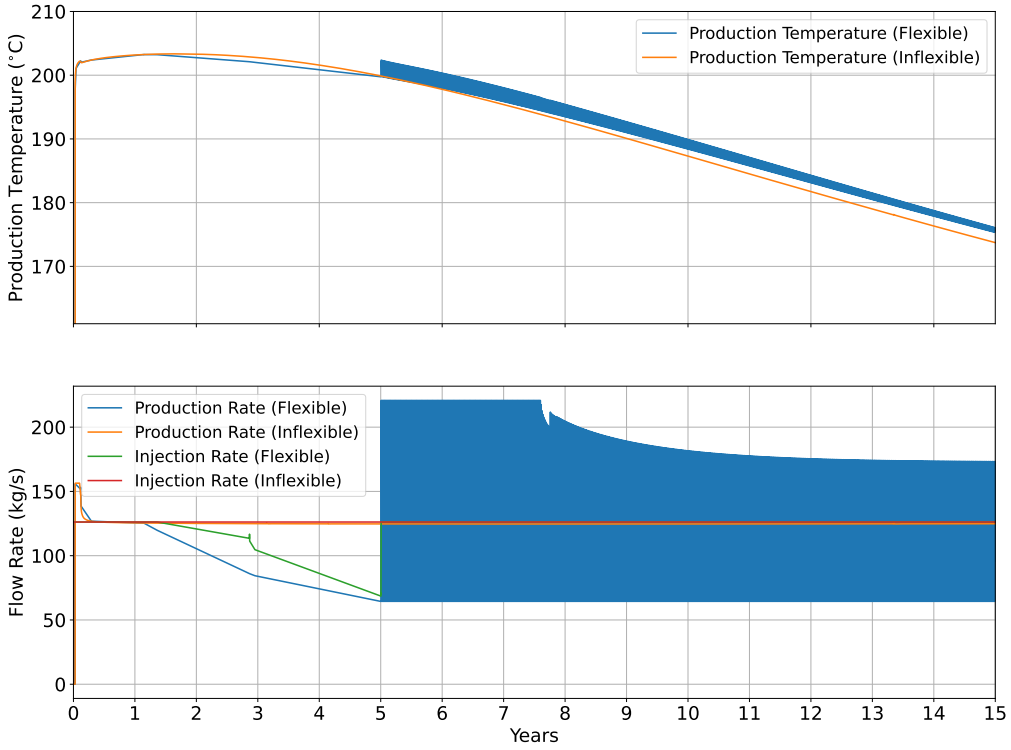

Supplementary Figure 35: Comparison of long-run thermal drawdown under cases where production flow rates are either held constant or cycled under a 40 hour choke / 80 hour open operating profile, and injection rates are held constant. Due to computational limitations, these simulations use a truncated reservoir design with 1/10 the lateral length and 2/3 the lateral offset of the standard design, and three simulated wells instead of five. The shorter lateral offset enables observation of a more significant thermal decline over a shorter simulated period. Note that while the simulated operational behaviors are not identical in the first five years, the final ten years of data show nearly identical decline profiles for cases with identical steady-state injection rates without noticeable deviations resulting from the flexible production strategy.

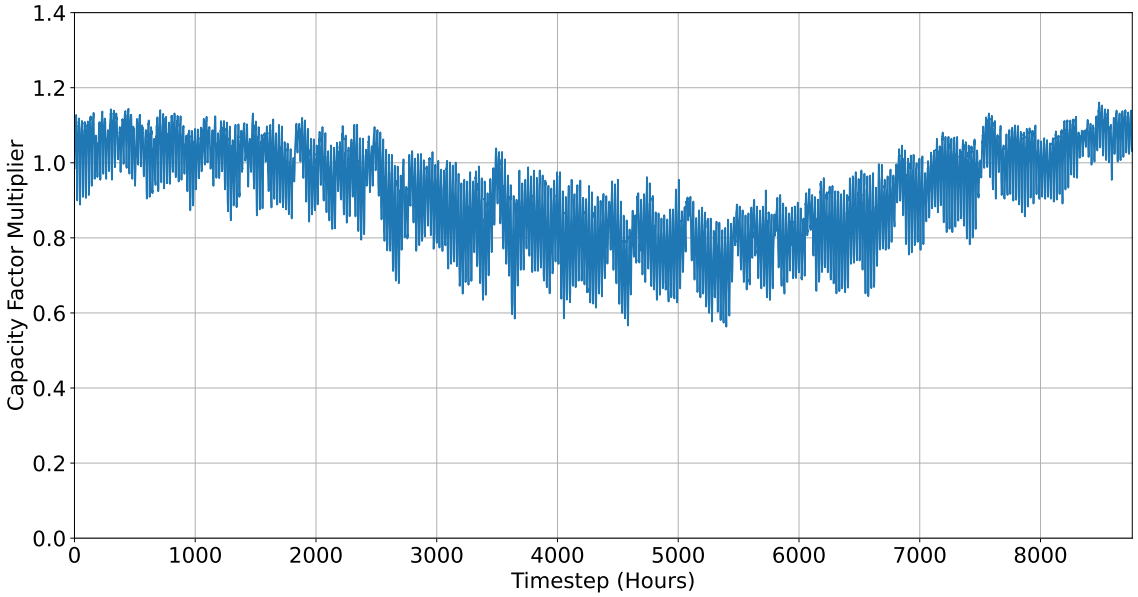

Supplementary Figure 36: Hourly capacity factor time series for an EGS plant in southern California (weather region 10).

Supplementary Note 7: EGS Supply Curves

We develop zonal supply curves for EGS resources at depths from 3.5 to 6.5 km and temperatures from 150 °C to 325 °C using modified resource potential estimates from Augustine [39], which are based on temperature-at-depth datasets from Blackwell et al. [40]. Resource potentials from Augustine [39] are available for each balancing area in the ReEDS CEM, and are binned by depth at 1 km intervals and by resource temperature at 25 °C intervals. They assume analytically determined volumetric electric power densities for EGS reservoirs in each temperature bin. For the present work we calculate reservoir electric power density directly using results from numerical reservoir simulations and GETEM. We assume a standard reservoir design consisting of four injection wells and five production wells, with a fracture network area of 5.57 km^2 in the horizontal plane. We assume that each reservoir occupies a 1 km vertical interval centered on the reservoir and a horizontal area five times the area of its fracture network, leading to a total extended volume of 27.84 km^3 per reservoir, or 6.96 km^3 per injection well. For each temperature bin, depth bin, region, and drilling scenario we calculate the net electric generating capacity of a standard reservoir using GETEM. Regional differences are determined by local average ambient temperature, as described in section 6. Average resource temperature in each bin is assumed to be 8 °C greater than the bin's lower bound, in line with trends observed in shallow temperature-at-depth datasets [41]. Electric generating capacity per reservoir is divided by extended reservoir volume to calculate volumetric electric power density. We modify resource potentials from Young et al. [42] by multiplying the total potential in each resource bin by the ratio of our calculated electric power density to the electric power density assumed in Young et al. [42]. Resource potentials calculated in Young et al. [42] and used in doe [28] do not consider depths less than 3.5 km. For shallower depths we calculate resource potentials directly using temperature-at-depth data from Mullane et al. [41]. We use exclusion zones for geothermal development from Young et al. [42], and additionally exclude large existing hydrothermal reservoirs at the Geysers and the Salton Sea. For the remaining resource, the total volume of each temperature and depth bin is measured directly and multiplied by electric power density to calculate resource potential. We include potential estimates for 1.5 km and 2.5 km reservoir depths.

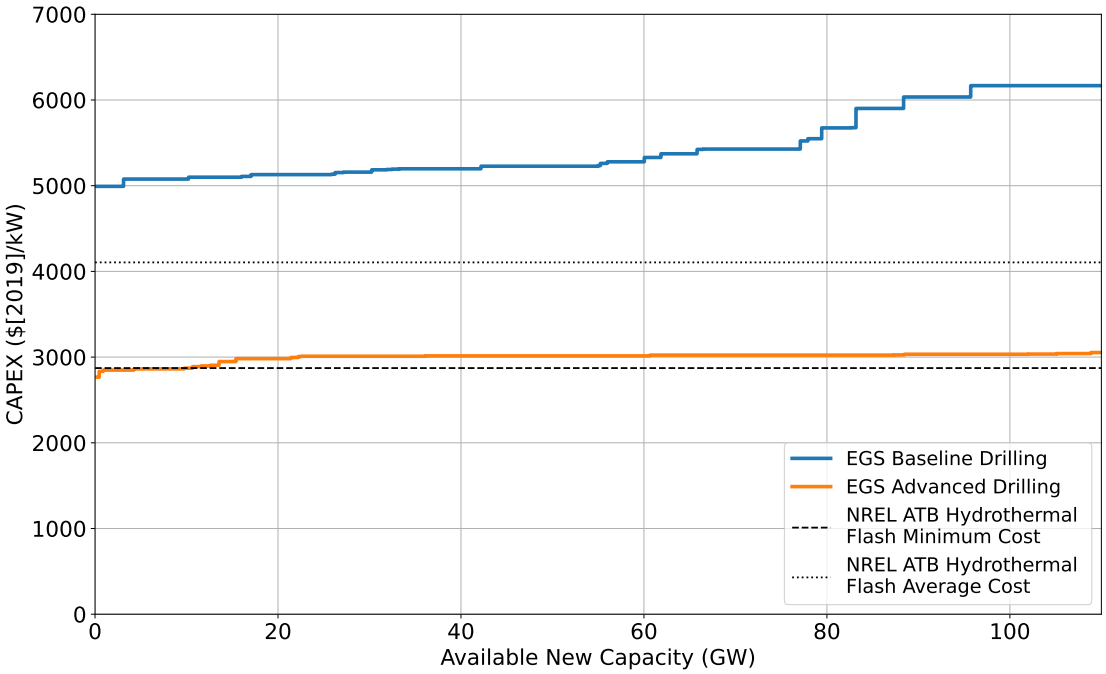

Supplementary Figure 37: Supply curves for EGS power in the United States Western Interconnection under Baseline and Advanced drilling scenarios. CAPEX is given with respect to plant net generating capacity (including steady-state injection load) at the local average ambient temperature, and does not include grid interconnection costs. Dotted lines indicating costs for conventional geothermal plants taken from the NREL ATB are shown for comparison purposes.

We use a transmission routing methodology developed in Jenkins et al. [43] to assign EGS resources to GenX model zones and calculate transmission interconnection costs. For deep resources (3.5 km

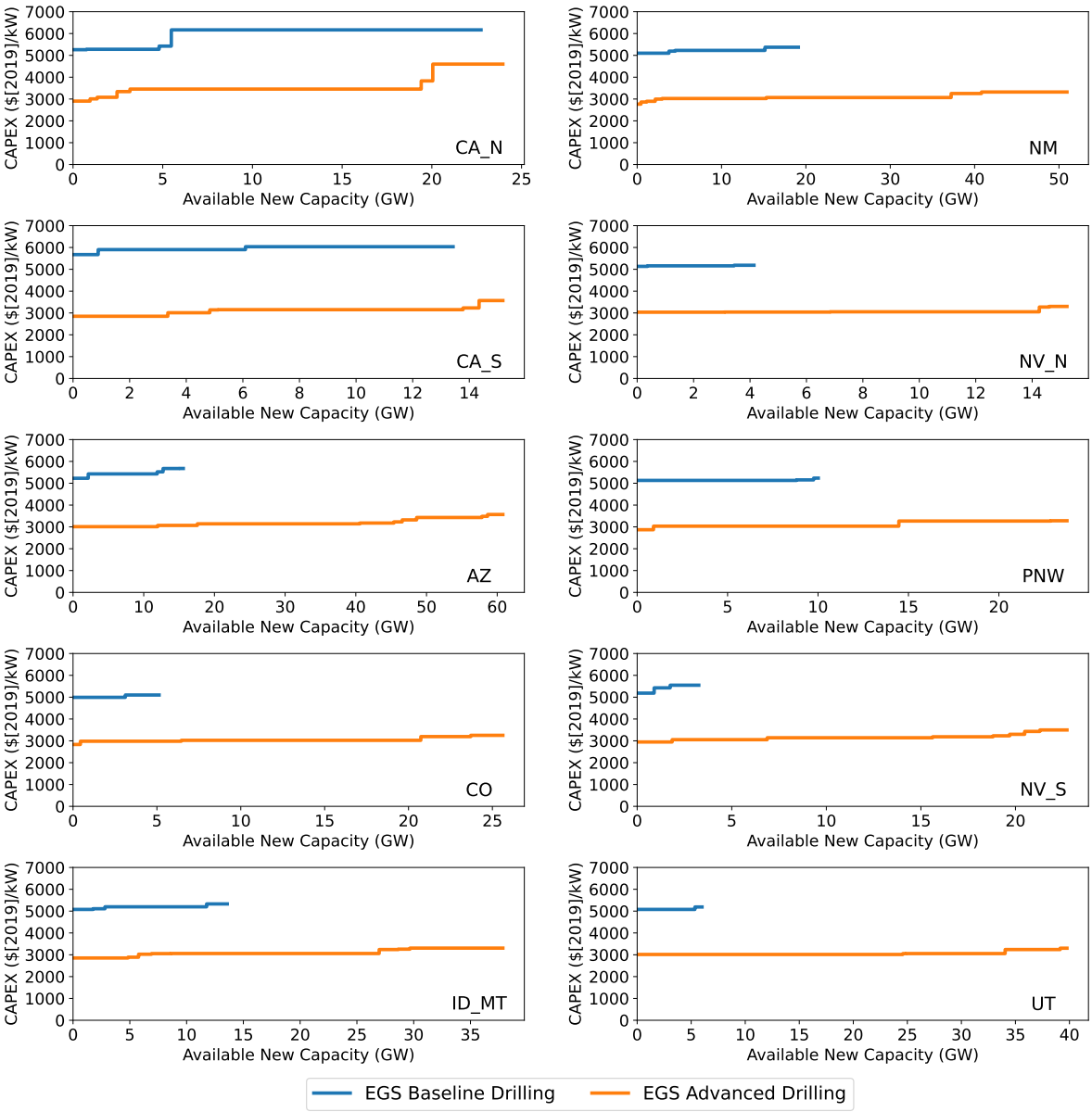

Supplementary Figure 38: Zonal supply curves used as GenX inputs in the baseline and advanced drilling cases. No EGS resources are developable in the GenX WY zone.

or greater), we use the underlying temperature-at-depth maps from Blackwell et al. [40] and exclusion layers from Young et al. [42] to map geothermal resource 'clusters' for each temperature/depth bin in each ReEDS balancing area. If clusters in a given temperature/depth bin are spatially non-contiguous, we divide these into multiple contiguous clusters and divide the total regional resource potential among these based on measured geographic area. For shallow resources, EGS clusters are mapped directly using temperature-at-depth maps from Mullane et al. [41] and the modified shallow exclusion zones described above. Shallow resources are also assigned to ReEDS balancing areas for the purpose of weather region mapping, which is described in section 6. Optimal transmission routes are calculated from each EGS cluster's centroid to major load centers based on transmission cost surface maps, and each cluster is assigned to the GenX model zone for which its interconnection cost is minimized. Some EGS resources are therefore assigned to GenX zones in which they are not physically located. Clusters with very large interconnection annuities (> \$100000/MW-yr) are excluded from the resource pool. Of the remaining clusters in each GenX zone, all that occupy the same temperature/depth bin and are physically located in the same ReEDS region are recombined into a single cluster, and the interconnection annuity for the combined cluster is set as the capacity-weighted average of interconnection annuities for the component clusters. In the interest of minimizing solution time we do not include comprehensive supply curves for all temperatures and depths, and instead include only the least-cost resources in each model region. We add resource clusters in order of annuitized fixed cost until the total available resource in each region significantly exceeds the expected buildout or the economical resource has been exhausted. Final supply curves for each drilling case are shown in Supplementary Figure 37. Regional supply curves are shown in Supplementary Figure 38. The Baseline Drilling supply curve, which only contains resources at temperatures < 250 °C, is fairly steep, and the total economically viable resource base is limited. The inclusion of resources at temperatures > 250 °C in the Advanced Drilling supply curve leads to a greatly expanded resource base, with significantly more high-quality capacity available than is deployed in any of our model scenarios.

Supplementary References

[1] J. Jenkins and N. Sepulveda, "Enhanced decision support for a changing electricity landscape: The genx configurable electricity resource capacity expansion model," MIT Energy Initiative, Cambridge, MA, Working Paper, 2017.

[2] "GenX," 2022. [Online]. Available: https://github.com/GenXProject/GenX

[3] W. Ricks, K. Voller, G. Galban, J. Norbeck, and J. Jenkins, "The Role of Flexible Geothermal Power in Decarbonized Electricity Systems: Supplementary Data," 2022.

[4] Gurobi Optimization, LLC, "Gurobi Optimizer Reference Manual," 2022. [Online]. Available: https://www.gurobi.com

[5] D. S. Mallapragada, N. A. Sepulveda, and J. D. Jenkins, "Long-run system value of battery energy storage in future grids with increasing wind and solar generation," *Applied Energy*, vol. 275, p. 115390, 2020. [Online]. Available: https://www.sciencedirect.com/science/article/pii/S0306261920309028

[6] "2020 Summer Reliability Assessment," North American Electric Reliability Corporation, Tech. Rep., 2020.

[7] National Conference of State Legislatures, "State Renewable Portfolio Standards and Goals," 2022. [Online]. Available: https://www.ncsl.org/research/energy/renewable-portfolio-standards.aspx

[8] G. Schivley, E. Welty, N. Patankar, A. Jacobson, Q. Xu, A. Manocha, and J. D. Jenkins, "PowerGenome/PowerGenome: v0.5.4," Feb. 2022. [Online]. Available: https://doi.org/10.5281/zenodo.6092712

[9] E. Larson, C. Greig, J. Jenkins, E. Mayfield, A. Pascale, C. Zhang, J. Drossman, R. Williams, S. Pacala, R. Socolow, E. Baik, R. Birdsey, R. Duke, R. Jones, B. Haley, E. Leslie, K. Paustian, and A. Swan, "Net-Zero America: Potential Pathways, Infrastructure, and Impacts," Princeton, NJ, 2020.

[10] T. Mai, P. Jadun, J. Logan, C. McMillan, M. Muratori, D. Steinberg, L. Vimmerstedt, R. Jones, B. Haley, and B. Nelson, "Electrification Futures Study: Scenarios of Electric Technology Adoption and Power Consumption in the United States," National Renewable Energy Laboratory, Golden, CO, Tech. Rep. NREL/TP-6A20-71500, 2018.

[11] Z. Selvans, C. Gosnell, A. Sharpe, S. Winter, J. Rousik, E. Welty, and B. Norman, "The Public Utility Data Liberation (PUDL) Project," Nov. 2021, If you use PUDL, please cite it as indicated below. [Online]. Available: https://doi.org/10.5281/zenodo.5677623

[12] "DOE Global Energy Storage Database," Sandia National Lab, 2021. [Online]. Available: https://sandia.gov/ess-ssl/gesdb/public/statistics.html

[13] "Form EIA-861M detailed data, January 2022," U.S. Energy Information Administration, 2022.

[14] S. Pfenninger and I. Staffell, "Long-term patterns of European PV output using 30 years of validated hourly reanalysis and satellite data," *Energy*, vol. 114, pp. 1251–1265, 2016. [Online]. Available: https://www.renewables.ninja

[15] "2021 Annual Technology Baseline," National Renewable Energy Laboratory, Golden, CO, Tech. Rep., 2021.

[16] "Cost and Performance Characteristics of New Generating Technologies, Annual Energy Outlook 2020," U.S. Energy Information Administration, 2020. [Online]. Available: https://www.eia.gov/outlooks/archive/aeo20/assumptions/pdf/table_8.2.pdf

[17] E. Baik, K. P. Chawla, J. D. Jenkins, C. Kolster, N. S. Patankar, A. Olson, S. M. Benson, and J. C. Long, "What is different about different net-zero carbon electricity systems?" *Energy and Climate Change*, vol. 2, p. 100046, 2021.

[18] V. Viswanathan, K. Mongird, R. Franks, X. Li, V. Sprenkle, and R. Baxter, "2022 Grid Energy Storage Technology Cost and Performance Assessment," Pacific Northwest National Lab, Richland, WA, Tech. Rep. PNNL-33283, 2022.

[19] "Annual Energy Outlook 2021," U. S. Energy Information Administration (EIA), Washington, D.C., Tech. Rep., 2021.

[20] J. Ho, J. Becker, M. Brown, P. Brown, I. Chernyakhovskiy, S. Cohen, W. Cole, S. Corcoran, K. Eurek, W. Frazier, P. Gagnon, N. Gates, D. Greer, P. Jadun, S. Khanal, S. Machen, M. Macmillan, T. Mai, M. Mowers, C. Murphy, A. Rose, A. Schleifer, B. Sergi, D. Steinberg, Y. Sun, and E. Zhou, "Regional Energy Deployment System (ReEDS) Model Documentation: Version 2020," National Renewable Energy Laboratory, Golden, CO, Tech. Rep. NREL/TP- 6A20-78195, 2021.

[21] W. Ricks, J. Norbeck, and J. Jenkins, "The value of in-reservoir energy storage for flexible dispatch of geothermal power," *Applied Energy*, vol. 313, p. 118807, 2022.

[22] D. Hu, Y. Zheng, Y. Wu, S. Li, and Y. Dai, "Off-design performance comparison of an organic rankine cycle under different control strategies," *Applied Energy*, vol. 156, pp. 268–279, 2015. [Online]. Available: https://www.sciencedirect.com/science/article/pii/S0306261915008582

[23] M. Karadas, H. M. Celik, U. Serpen, and M. Toksoy, "Multiple regression analysis of performance parameters of a binary cycle geothermal power plant," *Geothermics*, vol. 54, pp. 68–75, 2015. [Online]. Available: https://www.sciencedirect.com/science/article/pii/S0375650514001333

[24] C. Augustine, "A Methodology for Calculating EGS Electricity Generation Potential Based on the Gringarten Model for Heat Extraction From Fractured Rock," *GRC Transactions*, vol. 40, 2016.

[25] M. McClure and C. Kang, "A three-dimensional reservoir, wellbore, and hydraulic fracturing simulator that is compositional and thermal, tracks proppant and water solute transport, includes non-darcy and non-newtonian flow, and handles fracture closure," in *Presented at the SPE Reservoir Simulation Conference*, Montgomery, TX, 2017.

[26] M. McClure, C. Kang, C. Hewson, and S. Medam, "ResFrac Technical Writeup," ResFrac Corporation, Palo Alto, CA, Tech. Rep., 2021, https://www.resfrac.com/wp-content/uploads/2021/06/ResFrac-Technical-Writeup-February-13-2021.pdf.

[27] T. S. Lowry, J. T. Finger, A. Foris, M. B. Kennedy, T. F. Corbet, C. A. Doughty, S. Pye, and E. L. Sonnenthal, "GeoVision Analysis Supporting Task Force Report: Reservoir Maintenance and Development," Sandia National Laboratories, Albuquerque, NW, Tech. Rep. SAND2017-9977, 2017.

[28] "GeoVision," U.S. Department of Energy (DOE), Tech. Rep., 2019.

[29] F. Dupriest and S. Noynaert, "Drilling Practices and Workflows for Geothermal Operations," in *SPE/IADC Drilling Conference and Exhibition*, 2022.

[30] G. Mines, "GETEM User Manual," Idaho National Laboratories, Idaho Falls, ID, Tech. Rep. INL/EXT-16-38751, 2016.

[31] C. Augustine, J. Ho, and N. Blair, "GeoVision Analysis Supporting Task Force Report: Electric Sector Potential and Penetration," National Renewable Energy Laboratory, Golden, CO, Tech. Rep. NREL/TP-6A20-71833, 2019.

[32] "The Future of Geothermal Energy," Idaho National Laboratory, Idaho Falls, ID, Tech. Rep. INL/EXT-06-11746, 2006.

[33] B. Adams, J. Ogland-Hand, J. M. Bielicki, P. Schädle, and M. Saar, "Estimating the Geothermal Electricity Generation Potential of Sedimentary Basins Using genGEO (The Generalizable GEOthermal Techno-Economic Simulator)," 1 2021, preprint, DOI: 10.26434/chemrxiv.13514440.v1.

[34] S. Akar, C. Augustine, P. Kurup, and M. Mann, "Global value chain and manufacturing analysis on geothermal power plant turbines," in *Presented at the 41st Geothermal Resource Council Annual Meeting*, Salt Lake City, UT, 2017.

[35] H. Legmann, "The 100-MW Ngatamariki Geothermal Power Station: A Purpose-Built Plant For High Temperature, High Enthalphy Resource," in *Proceedings of the World Geothermal Congress 2015*, Melbourne, Australia, 2015.

[36] K. Beckers and K. McCabe, "GEOPHIRES v2.0: updated geothermal techno-economic simulation tool," *Geothermal Energy*, vol. 9, 2019.

[37] F. Belock and R. Mendes, "Water Tank Selection Comparison: Steel versus Prestressed Concrete," San Diego Water Department, San Diego, CA, Tech. Rep., 2005.

[38] "Hourly/Sub-Hourly Observational Data Version 3.0.0," 2021, National Oceanic and Atmospheric Administration, National Centers for Environmental Information. https://www.ncei.noaa.gov/maps/hourly/.

[39] C. Augustine, "Update to Enhanced Geothermal System Resource Potential Estimate," 2016, National Renewable Energy Laboratory. Presented at the 40th GRC Annual Meeting, Sacramento, CA, 2016.

[40] D. Blackwell, M. Richards, Z. Frone, J. Batir, A. Ruzo, R. Dingwall, and M. Williams, "Temperature-At-Depth Maps for the Conterminous U. S. and Geothermal Resource Estimates," *GRC Transactions*, vol. 31, pp. 1545–1550, 2011.

[41] M. Mullane, M. Gleason, K. McCabe, M. Mooney, T. Reber, and K. Young, "An Estimate of Shallow, Low-Temperature Geothermal Resources in the United States," 2016, National Renewable Energy Laboratory. Presented at the 40th GRC Annual Meeting, Sacramento, CA, 2016.

[42] K. Young, A. Levine, J. Cook, D. Heimiller, and J. Ho, "GeoVision Analysis Supporting Task Force Report: Barriers," National Renewable Energy Laboratory, Golden, CO, Tech. Rep. NREL/TP-6A20-71641, 2019.

[43] J. D. Jenkins, E. N. Mayfield, J. Farbes, R. Jones, N. Patankar, Q. Xu, and G. Schivley, "Preliminary Report: The Climate and Energy Impacts of the Inflation Reduction Act of 2022," REPEAT Project, Tech. Rep., 2022.